Journal of the European Ceramic Society 41 (2021) 18–33

Contents lists available at ScienceDirect

Journal of the European Ceramic Society

journal homepage: www.elsevier.com/locate/jeurceramsoc

Review article

Rheological characterisation of ceramic inks for 3D direct ink writing: A review

Laura del-Mazo-Barbara [a,b,c], Maria-Pau Ginebra [a,b,c,d,*]

[a] Biomaterials, Biomechanics and Tissue Engineering Group, Department of Materials Science and Engineering, Universitat Politècnica de Catalunya (UPC), EEBE, Av. Eduard Maristany, 16, 08019 Barcelona, Spain
[b] Barcelona Research Centre for Multiscale Science and Engineering, Universitat Politècnica de Catalunya (UPC), EEBE, Av. Eduard Maristany, 10-14, 08019 Barcelona, Spain
[c] Biomedical Engineering Research Center (CREB), Universitat Politècnica de Catalunya, Av. Diagonal, 647, 08028 Barcelona, Spain
[d] Institute for Bioengineering of Catalonia (IBEC), Barcelona Institute of Science and Technology, Baldiri Reixac 10- 12, 08028 Barcelona, Spain

ARTICLE INFO

Keywords:
3D printing
Direct Ink Writing
Robocasting
Rheology
Printability

ABSTRACT

3D printing is a competitive manufacturing technology, which has opened up new possibilities for the fabrication of complex ceramic structures and customised parts. Extrusion-based technologies, also known as direct ink writing (DIW) or robocasting, are amongst the most used for ceramic materials. In them, the rheological properties of the ink play a crucial role, determining both the extrudability of the paste and the shape fidelity of the printed parts. However, comprehensive rheological studies of printable ceramic inks are scarce and may be difficult to understand for non-specialists. The aim of this review is to provide an overview of the main types of ceramic ink formulations developed for DIW and a detailed description of the more relevant rheological tests for assessing the printability of ceramic pastes. Moreover, the key rheological parameters are identified and linked to printability aspects, including the values reported in the literature for different ink compositions.

1. Introduction

Three-dimensional (3D) printing is an emerging manufacturing technology that enables the fabrication of geometrically complex structures with high resolution and minimum material waste, which is difficult to achieve by conventional methods such as casting and machining [1]. In this approach, 3D parts are built from computer-aided design (CAD) models by adding material layer by layer, which is why it is also called additive manufacturing (AM) [1].

Substantial advances have been made in recent years in AM, especially in the field of polymeric [2–4] and metallic materials [5,6]. However, the application of AM to ceramics is more challenging, due to its inherent high melting point [7]. In fact, the design and development of advanced ceramics by AM for high-performance applications is one of the most challenging tasks of modern engineering [8].

Several methods have been proposed for 3D-printing of ceramic materials, which include: (i) Vat polymerisation, based on the layer by layer UV-light polymerisation of a photocurable liquid vat highly loaded with ceramic particles, trapping the ceramic powder within the cross-linked polymer network; (ii) Powder bed based methods, consisting in the layer by layer consolidation of a ceramic powder bed using different strategies, such as sintering local regions with a laser beam (Selective Laser Sintering - SLS), or spraying one or more binders from inkjets (Binder Jetting or 3D-Plotting); and (iii) Material extrusion, also known as Direct Ink Writing (DIW) or robocasting, based on the extrusion of a flowable ceramic paste or ink through a nozzle, and building a 3D part by stacking filaments (Fig. 1). Alternatively, the ceramic powder can be included in a filament of a thermoplastic polymer and processed by fused deposition modelling (FDM), where the extrusion is done using a heated nozzle that melts the polymer [9].

DIW offers the ability to rapidly fabricate complex structures of a wide range of ceramic materials at a relatively low cost, and is among the most used AM techniques for ceramic manufacturing in a variety of applications. The nozzles can vary greatly in size, ranging from nozzle diameters as small as 0.1 μm used in microfabrication [10] to nozzles as big as several dm for concrete printing in building applications [11,12].

Ceramic inks for DIW consist of highly concentrated suspensions of ceramic particles, which are also known as ceramic pastes or slurries. A

* Corresponding author. Present address: Department of Materials Science and Engineering, Universitat Politècnica de Catalunya (UPC), Av. Eduard Maristany, 16, 08019 Barcelona, Spain.
E-mail address: maria.pau.ginebra@upc.edu (M.-P. Ginebra).

https://doi.org/10.1016/j.jeurceramsoc.2021.08.031
Received 31 May 2021; Received in revised form 13 August 2021; Accepted 16 August 2021
Available online 18 August 2021

wide range of ceramic pastes have been developed as DIW inks for bone tissue engineering, structural, electronic and optical applications, as summarised in Table 1.

The design of the ink represents the most critical aspect of DIW. An adequate ink for DIW requires a good homogeneity, a high enough ceramic charge to minimize shrinkage, and appropriate rheological properties to be extruded and at the same time guarantee the required shape fidelity and structural stability once deposited.

The aim of this article is to provide an overview of the most recent advances on DIW of ceramics, focusing on the characterisation and optimisation of the rheological properties of the ceramic inks and its relation with the printability assessment.

Table 1
Main applications of DIW with ceramic inks, including some relevant publications.

Field		Ref.
Bone Tissue Engineering		[9,13–38]
Structural Components		[39–45]
Electronics	Energy Storage Devices	[46,47]
	Advanced Wearable Devices	[48]
	Piezoelectric Components	[49–51]
Microwave Optics		[52]

2. Ceramic inks for direct ink writing

The DIW printing process imposes stringent requirements on the rheological behaviour of the inks. On the one hand, the ink must be smoothly extruded through a narrow nozzle without clogging to form continuous filaments. On the other hand, after being extruded the filaments must be able to retain the shape of the nozzle, accurately reproduce the printing path and support layer stacking to avoid the collapsing of the 3D printed structure. In order words, the ink has to be extrudable, have shape-retention capacity and be self-supporting (Fig. 2).

As will be described in detail later, to fulfil these requirements ideally the DIW ink should behave like a fluid during the extrusion process, and exhibit an elastic behaviour once it is at rest and the applied stresses cease. Two main approaches have been undertaken to obtain ceramic inks that show this rheological behaviour, colloidal suspensions and gel-embedded suspensions, which include either hydrogel or organogel based suspensions (Fig. 3). Their main characteristics and distinguishing features are summarised below, and representative examples of ceramic ink formulations developed for various applications are displayed in Table 2.

Colloidal suspensions are highly concentrated slurries of ceramic particles (typically 40−50 vol.% or 60−80 wt.%) in a low-viscosity liquid, commonly water, and a small portion of organic additives (<2 vol. % [53,54] or ≤ 1 wt.% [19,20]) that allow tuning the interaction forces between particles by electrostatic, steric or electrosteric mechanisms [7,27]. Polyelectrolyte species with amine or carboxylic groups, such as polyacrylate (PAA), polyvinyl alcohol (PVA), and polyethyleneimine (PEI) have been commonly used to stabilize ceramic particles. Using an adequate solid loading and tailoring the interparticle interactions in the ceramic suspension it is possible to enable the extrusion process while ensuring the structural integrity of the ink after deposition, owing to a gelling process. Moreover, extrudability can be enhanced by the addition of dispersant or plastifying agents, such as cellulose-based polymers. The main drawback of this approach is that these inks may be very sensitive to variations on the chemistry and pH of the environment, making them unstable and difficult to control.

Gel-embedded suspensions have recently emerged as an alternative to colloidal suspensions for DIW applications. The main difference between them is that the rheological properties of gel-embedded suspensions do not derive directly from the particle-particle interactions, but from the properties of a gel phase where the particles are dispersed. This results in more stable suspensions, although it comes at the cost of reducing the solid loading of the inks. Hydrogels, such as those based on poloxamer 407 (Pluronic® F127) and cellulose, are the most usual choice due to their easy manipulation and the low volatility of water compared to other solvents. Although being less common, organogels (i.e., gels composed of a polymer dissolved in an organic solvent) are also explored in the literature [25,55]. Most of them rely on the liquid to solid transition through solvent evaporation just after the filament is deposited [56]. Different biopolymers have been studied such as poly(L-lactic acid) (PLLA), poly(lactic-co-glycolic acid) (PLGA), polyethylene glycol (PEG) and polycaprolactone (PCL) (Table 2). Since the behaviour of gel-embedded suspensions is not based on the surface chemistry of the particles, this approach has the advantage of being potentially compatible with any ceramic powder [57].

Finally, it is important to bear in mind that, after printing, the green bodies obtained need to be hardened through post-printing treatments. In general, the as-printed ceramic structures have to be subjected to drying and thermal debinding treatments to eliminate the organic components, followed by a sintering process. Unfortunately, this leads to a significant shrinkage, which may vary depending on the organic

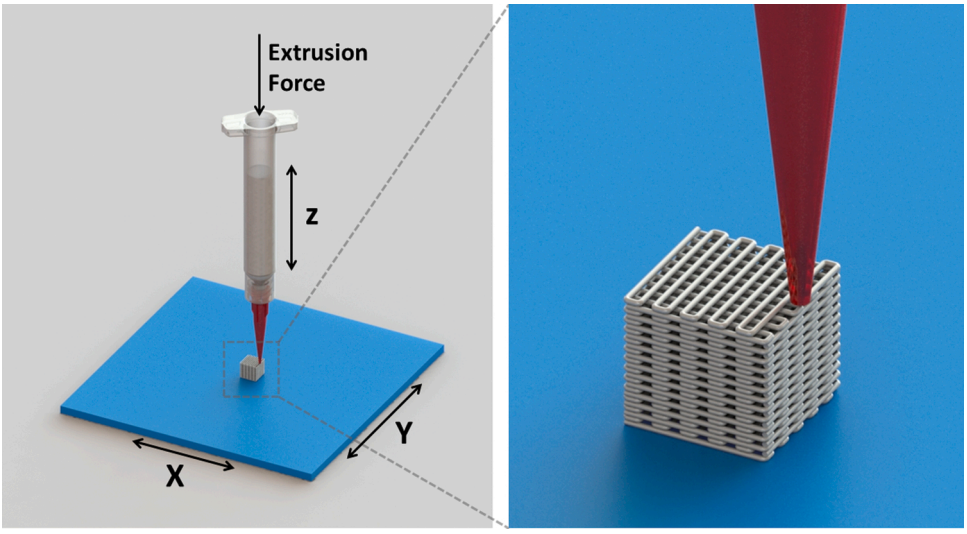

Fig. 1. Schematic illustration of the Direct Ink Writing (DIW) technology.

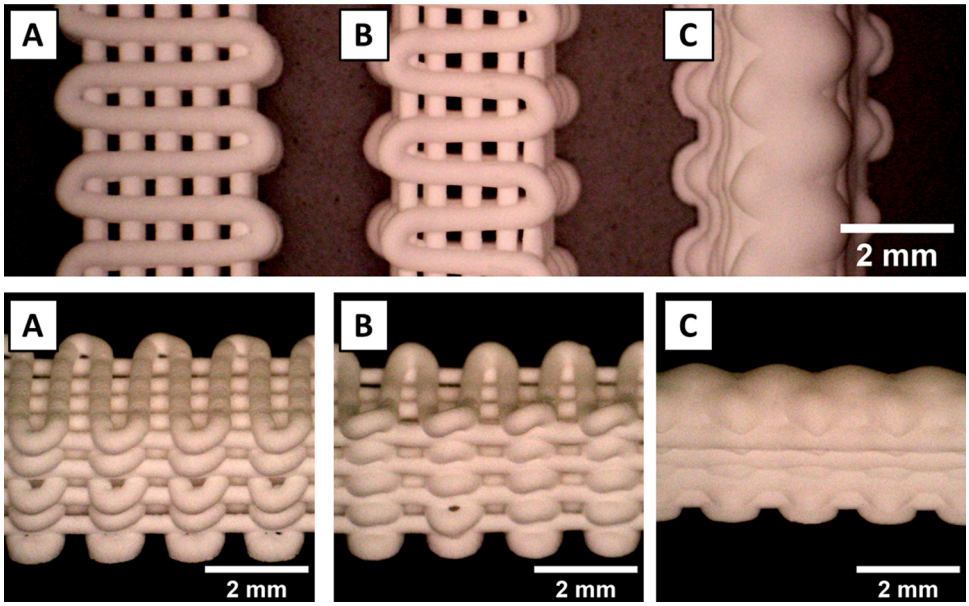

Fig. 2. Illustrative images of the concept of shape fidelity. The same pattern printed with three ceramic inks with different rheological properties. A) ceramic ink with good shape-retention and self-supporting capacity. B) sub-optimal ceramic ink, showing deficient shape-retention and self-supporting capacity. C) ink with inappropriate rheological properties, lacking shape-retention ability and self-supporting capacity.

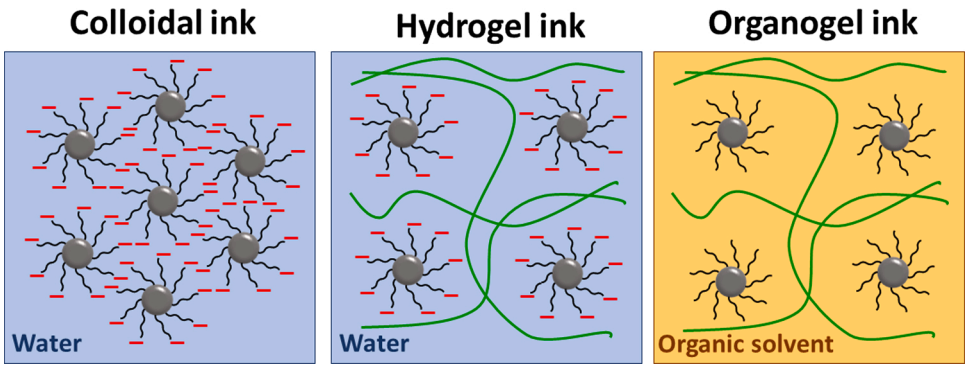

Fig. 3. Schematic diagram illustrating the interparticle interactions for the three main types of ceramic inks for DIW: colloidal, hydrogel and organogel based suspensions. The steric stabilisation mechanisms are represented with black lines and the electrostatic interactions with negative charges in red, which give rise to polyelectrolyte complexes in the colloidal inks. The polymer chains are symbolized by green lines in the gel-embedded inks. Adapted with permission from Ref. [7]. (For interpretation of the references to colour in this figure legend, the reader is referred to the web version of this article.)

fraction and the printing process [21,38,54,109]. Interestingly, there are alternative formulations of reactive ceramic inks that are able to self-set through a cement-like reaction, leading to the hardening of the parts at low temperature with a minimum shrinkage [13,14,109].

3. Basic concepts of rheology

During the DIW process, the ink is forced to flow through a nozzle under an applied stress. The rheological properties of the flowable paste are of paramount importance since they will determine both the extrusion process and the behaviour of the filament after extrusion. In the following sections the fundamentals of viscous and viscoelastic behaviours are briefly described.

3.1. Viscous behaviour

The molecules within a fluid do not have defined positions as the atoms within a solid. As a consequence, when subjected to a shear stress, it flows (irreversible deformation), whereas a solid material deforms in a spring-like manner (elastic deformation) due to the inter-atomic bonds [110]. However, a viscous material offers some resistance to flow, called viscosity, which stems from the internal friction between adjacent layers of fluid that are in relative motion.

3.1.1. Effect of shear rate on viscosity: Newtonian, Pseudoplastic and Dilatant materials

The flow of a fluid is opposed by the friction between adjacent layers in relative motion, and therefore a force is required to sustain the fluid flow. The flow behaviour of a viscous material is described by the Ostwald-de Waele power law, for which shear stress (τ) is given by shear rate:

$$\tau = k\cdot(\dot{\gamma})^{n} \quad (1)$$

where $\dot{\gamma}$ is the shear rate, k the flow consistency parameter and n the flow behaviour index. The apparent viscosity η is a parameter that, in general, depends on the shear rate and is defined as

$$\eta = k\cdot(\dot{\gamma})^{n-1} \quad (2)$$

And therefore, combining Eqs. (1) and (2)

$$\tau = \left[k\cdot(\dot{\gamma})^{n-1}\right](\dot{\gamma}) = \eta\cdot(\dot{\gamma}) \quad (3)$$

Depending on the value of the flow behaviour index, viscous materials can be classified in: Newtonian, when $n = 1$ and the viscosity is constant and independent of the shear rate; pseudoplastic or shear-thinning, when $0 < n < 1$; and dilatant or shear-thickening, when $n > 1$, as represented in Fig. 4.

In pseudoplastic materials the viscosity decreases as the shear rate

Table 2
Composition of different ceramic inks developed for Direct Ink Writing, based either on colloidal suspensions or on gel-embedded suspensions.

Type	Binder Solvent	Additives	Ceramic Powder Type	Content	Ref.
Colloidal	Water		Boehmite	43–45 wt.%	[39]
		Sodium silicate, Graphene oxide	Kaolin clay	62.5 wt.%	[43]
		Sodium silicate	Kaolin clay	*23.81 wt.%*	[58]
		Sodium silicate, Polyelectrolyte dispersant	Kaolin clay	45 wt.%	[44]
				32 vol.%	[59]
				50/53 vol.%	[60]
		Polyelectrolyte dispersant	Alumina	58–61 vol.%	[53]
		Valeric/Propionic acid	Alumina	38–42 vol.%	[54]
		Polyelectrolyte dispersant	Calcium phosphate	48 vol.%	[61]
				49 vol.%	[23]
			Mullite	52 vol.%	[62]
			Lead zirconate titanate	45 vol.%	[63]
		Sodium citrate dispersant	Lead lanthanum zirconate titanate	70 vol.%	[50,51]
		Polyethyleneimine	Boron carbide	54 vol.%	[45]
		Cellulose, Polyelectrolyte dispersant	Lead zirconate titanate	47 vol.%	[27,64]
		Methylcellulose, Polyelectrolyte dispersant	Alumina	47 vol.%	[54]
		Hydroxypropyl methylcellulose (0.9 wt.%), Polyethyleneimine (5 wt.%)	Silicon nitride	61.8 wt.%	[65]
		Hydroxypropyl methylcellulose, Polyethyleneimine, Polyelectrolyte dispersant	Calcium phosphate	35 vol.%	[66,67]
				45 vol.%	[19,66]
				46 vol.%	[68]
				48/53 vol.%	[28]
				49.2/51 vol.%	[69]
				40 wt.%	[20]
			Lead-free barium zirconate titanate	40–44 vol.%	[57,70]
			Titania	45.2 vol.% (*76.05 wt.%*)	[57]
			Zirconia	43.6 vol.% (*80.49 wt.%*)	[57]
			Barium titanate	47 vol.%	[71]
			Strontium titanate	47 vol.%	[71]
			Barium zirconate	47 vol.%	[71]
			Zirconia	41 vol.% (83.5 wt.%)	[72]
		Ethyl-hydroxyethyl-cellulose (0.42 wt.%), Ammonium acetate, Polyelectrolyte dispersant	Alumina	52 vol.% (81 wt.%)	[73]
		Ethyl-hydroxyethyl-cellulose (*0.42 wt.%*), Polyethyleneimine (*0.9 wt.%*), Polyelectrolyte dispersant (*0.4 wt.%*)	Alumina	49.9 vol.% (79.6 wt.%)	[74]
		Methylcellulose (15 mg/ml[a]), Polyethyleneimine, Polyelectrolyte dispersant	Alumina	40 vol.%	[75,76]
		Methylcellulose (1.6 wt.%[a]), Propylene carbonate (0.9 wt.%[a]), Diisononyl phthalate (1.3 wt.%[a]), Ammonium lauryl sulphate (<0.5 wt.%[a]), Ethylene glycol diacetate dispersant (3.3 wt.%[a])	Silver dimolybdate	78.96 wt.%	[77]
		Methylcellulose ($5_{wt.}$%[a]), Oligomeric polyester dispersant	Calcium phosphate	62.5 wt.%	[22]
				30 vol.%	[78]
			Carbon black	10 vol.%	[78]
		Carboxymethyl cellulose (1 wt.%), Poly(methyl vinyl ether) dispersant	Bioactive glass	45 vol.%	[35,79]
		Sodium tripolyphosphate (*2.43 wt.%*), Carboxymethylcellulose sodium salt (*0.36 wt.%*)	Calcium phosphate	*72.96 wt.%*	[18]
		Polyethyleneimine (0.5 mg/m^2 [d])	Silica	46 vol.%	[80]
		Polyvinyl alcohol (1 wt.%), Propionic acid	Alumina	46 vol.%	[54]
		Polyvinyl alcohol, Cross-linking agent, 1-octanol, Polyelectrolyte dispersant	Alumina	45.0–46.8 vol.%	[81]

(*continued on next page*)

Table 2 (*continued*)

Type	Binder Solvent	Additives	Ceramic Powder Type	Content	Ref.
		Polyvinyl alcohol (0.35–0.5 wt.%[c]), Polyethylene glycol (0.25 wt.%[c]), L-ascorbic acid or citric acid dispersant (0.2 wt.%[c])	Yttria-stabilized zirconia	34.2/37.7 vol.% (74.94/77.27 wt.%)	[42]
		Acrylamide monomer (*2.18 wt.%*), N,N′-methylenebisacrylamide (*0.29 wt.%*), Ammonium citrate dispersant (*1.63 wt.%*)	Calcium phosphate	52 vol.% (*79.96 wt.%*)	[82]
		Polyvinylpyrrolidone, Polyelectrolyte dispersant	Alumina	55 vol.%	[41]
		Alginic acid, Polyelectrolyte dispersant	Alumina	45 vol.%	[83]
		Sodium alginate (*0.05 wt.%*), Sodium hexametaphosphate dispersant (*0.3 wt.%*)	Titania	64–72 wt.%	[38]
	Aqueous solution of phosphoric acid and sodium hydroxide		Magnesium hydroxide	*18.57–22.06 mg/ml*[b]	[84]
	Aqueous solution of short-chain triglyceride, tween 80 and amphisol A		Calcium phosphate	80 wt.%	[26,85,86,87]
	α-terpineol	Ethyl cellulose (5 vol.%[a]), Dispersant	Lead niobium zirconate titanate	35 vol.%	[88]
Hydrogel		Polyvinyl alcohol (7.7 wt.%[b]), Polyethylene glycol (3.85 wt.%[b])	Titanium aluminum carbide	80.7 wt.%[b]	[89]
		Polyvinyl alcohol (2.91 wt.%[c])	Silicon nitride	46.55 wt.%	[90]
		Polyvinyl alcohol (6 wt.%[a])	Magnesium-doped wollastonite, Calcium phosphate	*56.52 wt.%*	[16]
			Silicon carbide	*57.45 wt.%*	[91]
		Pluronic F127 (20 wt.%[a])	Bioactive glass	30 vol.% 40 vol.%	[29] [92]
		Pluronic F127 (25 wt.%[a])	Bioactive glass	45 vol.%	[31,93]
			Silicon carbide	36 vol.%	[40]
			Alumina	39 vol.% 31 vol.% (65 wt.%)	[40] [94]
			Ceria-stabilized zirconia, Alumina	35 vol.%	[37]
		Pluronic F127 (30 wt.%[a])	Aluminum	20.7 $_{vol.}$% (*47.85 wt.%*)	[57]
			Calcium phosphate	*60.61 wt.%* *66.67 wt.%*	[95] [14]
		Pluronic F127 (10/20/30 wt.%[a]), Corn syrup, 1-Octanol	Calcium phosphate	32.92–51.91 vol.%	[21,96]
		Pluronic F127 (40wt/vol.% in PBS[a])	Calcium phosphate	*70 wt.%*	[97]
		Collagen (4 wt.%[a])	Calcium phosphate	80 vol.%	[98,99]
		Gelatine (10 wt.%[a])	Calcium phosphate	*1.54 g/ml*[a]	[13]
	30% ethanol	Hydroxypropyl methyl cellulose (1 wt.%[a])	Calcium phosphate	*60.60-64.52 wt.%*	[100,101]
		Gelatine (0-9 wt.%[c]), Hydroxypropyl methyl cellulose (1 wt.%[b])	Magnesium phosphate	*56.52 wt.%*	[102]
Organogel	Ethanol	Ethyl cellulose, (20.1/12.8 vol.%), Polyethylene glycol (6.8/4.3 vol.%)	Bioactive glass	45/40 vol.%	[34]
	Dichloromethane, 2-butoxyethanol, Dibutyl phthalate (weight ratio: 10:2:1)	Polycaprolactone (10/50 wt.%[c])	Calcium phosphate	1ml of ceramic/0.6 g of 2-butoxyethanol	[25]
		Poly lactic-co-glycolic acid (10wt.%[c])	Calcium phosphate	1ml of ceramic/0.6 g of 2-butoxyethanol	[25]
	Dichloromethane, $C_{27}H_{31}N_5$, dibutyl phthalate (weight ratio of 10:2:1)	Polycaprolactone (30 wt.%[c])	Magnesium phosphate	*63.00 wt.%*	[55]
	2-Propanol	Polyvinyl butyral (48-82 vol.%[b]), Polyethylene glycol (48–82 vol.%[b])	Alumina	29–49 vol.%[b]	[56]
			Lanthanum magnesium titanate	37–63 vol.%[b]	[56]
			Quartz	34–61 vol.%[b]	[56]
			Graphite	71–78 vol.%[b]	[56]
		Polyvinyl butyral (5.06 wt.%), Polyethylene glycol (1.65 wt.%)	Calcium phosphate	*28.58 wt.%*	[103]

(*continued on next page*)

Table 2 (*continued*)

Type	Binder Solvent	Additives	Ceramic Powder Type	Content	Ref.
		Polymethylsilsesquioxane (20.3/26.4 wt.%), Fumed silica (1.9/2.5 wt.%)	Zinc oxide, Calcium carbonate, Hardystonite	*65.5/57.7 wt.%*	[104]
	2-Propanol (2.5/2.5/2.3 vol.%), Toluene, (15/15/13.4 vol.%)	Boro-Polycarbosiloxane (20/20/32.3 vol.%), Uncured silicone (8.5/8.5/13.4 vol.%)	Silicon carbide, Yttrium-aluminum garnet	*54/54/38.4 vol.%*	[52]
	N-hexane	Polycarbosilane (precursor of silicon carbide)		70–80 wt.%	[105]
	n-methyl-2-pyrrolidone	Polystyrene-polyisoprene-polystyrene (3–10 vol.%)	NiZn-ferrite	58 vol.%	[106]
	Odorless mineral spirits water	Highly liquid paraffin, Palm wax, D(+)-sucrose	Alumina	23/31 vol.%	[107]
	Glycerol		Bismuth telluride	*50/55.56 wt.%*	[108]
		*inorganic binder: Antimony telluride chalcogenidometallate (*5.88/11.11/15.79 wt.%*)	Bismuth telluride	*47.06/44.44/42.11 wt.%*	[108]

Values in italics are self-calculations from the data provided in the respective article.
[a] Related to the Binder.
[b] Related to the solvent.
[c] Related to the solids.
[d] Related to the ceramic powder. In absence of superindex the percentage is related to the total volume or mass of the ink.

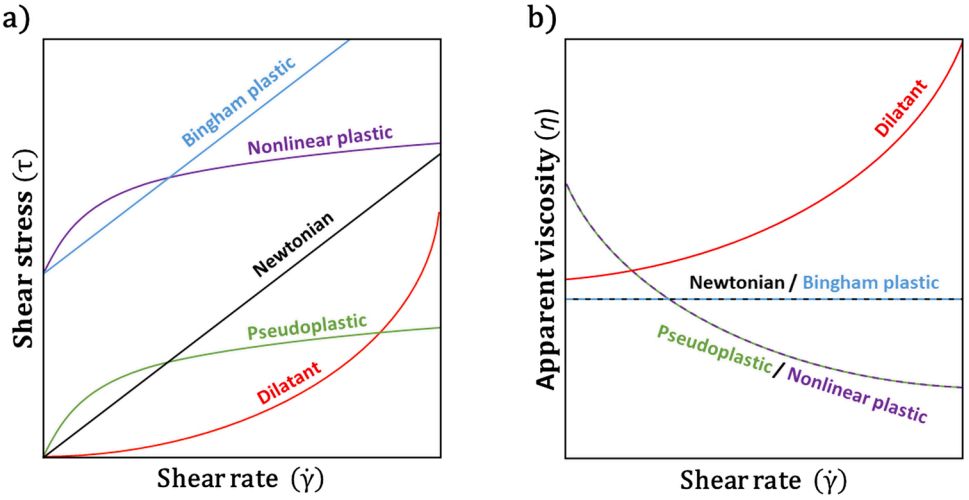

Fig. 4. Viscous materials: Newtonian (black), pseudoplastic (green), dilatant (red), Bingham plastic (blue) and nonlinear plastic (purple). a) shear stress versus strain. b) apparent viscosity versus shear rate. (For interpretation of the references to colour in this figure legend, the reader is referred to the web version of this article.)

increases (Fig. 4b). This is often observed in quotidian products such as creams and paints, the viscosity of which is much higher at rest than when applying them onto a wall or skin, with a high shear rate. This is caused by the disruption of interactions within the fluid or the ordering of the molecules or particles in the direction of the flow from an initial disordered state at rest.

Dilatant fluids exhibit the opposite behaviour, the viscosity increases as shear rate increases (Fig. 4b). This effect is rarely observed in daily products but it can be found in highly concentrated suspensions, e.g. corn starch [111].

Fig. 4 displays two additional behaviours. Some fluids do not start flowing unless the applied stress exceeds a certain critical value, known as yield stress (τ_y) [112]. In the case of nonlinear plastic fluids, the flow behaviour can be described by Herschel-Buckley model (Eq. (4)) [113].

$$\tau = \tau_y + k\cdot(\dot{\gamma})^n \quad (4)$$

If they exhibit a linear Newtonian behaviour (n = 1) when the shear stress exceeds the τ_y, they are called Bingham plastics.

3.1.2. *Time-dependent viscosity: Newtonian, Thixotropic and Rheopectic materials*

Besides the previously described dependence on shear rate, viscosity may also exhibit a dependence with the shearing time at a constant shear rate. In this respect, viscous materials can be classified into Newtonian, thixotropic or rheopectic. A newtonian fluid, like water, has a constant viscosity that is independent not only of the shear rate, but also of the sharing time. In contrast, when a constant shear stress is applied to a thixotropic fluid, the viscosity decreases with time, as a result of the progressive breakage of the internal attractive interactions by the continuous stress application [114]. This is frequently observed in quotidian products such as ketchup and yogurt that the longer they are shaken the lower the viscosity becomes. Finally, the opposite behaviour is found in rheopectic fluids, in which the viscosity increases with the time of application of the shear stress. This is a rather uncommon behaviour, shown by a limited number of fluids, such as gypsum and some lubricants, and is associated to shear-induced microstructural consolidation of the material [115]. The thixotropic and rheopectic effects can be reversed when the applied shear stress is decreased or removed, although it can require significant time to fully recover [114]

3.2. Viscoelastic behaviour

Many non-Newtonian fluids are viscoelastic, exhibiting a combination of elastic (solid-like) and viscous (fluid-like) behaviour. When a constant stress is applied, they suffer an instantaneous deformation as a result of the stretching of the interatomic or intermolecular bonds, but also a time-dependent deformation, as a result of the flow of atoms or molecules. When the stress is removed, only the elastic part of the total deformation is recovered instantaneously, followed by a progressive recovery over time of the viscous component, until an equilibrium state, which can be a complete recovery or not [110].

Viscoelasticity is often studied by applying a small oscillatory stress $\tau(t)$ and measuring the resulting strain $\gamma(t)$. In purely elastic materials the stress and strain are in phase, since the deformation is instantaneous. In purely viscous materials, there is a 90-degree strain lag. Viscoelastic materials exhibit a behaviour somewhere in the middle, as represented in Eqs. (5) and (6).

$$\gamma(t) = \gamma_0 \cdot \sin(2\pi f t) \tag{5}$$

$$\tau(t) = \tau_0 \cdot \sin(2\pi f t + \delta) \tag{6}$$

where γ_0 is the amplitude strain, f the frequency, τ_0 the amplitude stress and δ the phase angle, which will be 0° for purely elastic materials and 90° for purely viscous materials.

The complex modulus G^* is calculated by dividing the stress by the strain in the oscillatory test and represents the resistance of the material to deform. It can be decomposed in two components:

- the storage modulus G' that corresponds to $G^* \cdot \cos(\delta)$ and represents the elastic behaviour of the material. It is associated to the elastic stretching of the internal bonds, which results in deformation energy stored in the material.
- the loss modulus G'' that corresponds to $G^* \cdot \sin(\delta)$ and represents the viscous behaviour of the material, which arises from the internal friction between the components in a flowing fluid and is associated to the energy dissipated in the process, that cannot be recovered.

When G' is larger than G'' the material has a solid-like behaviour, whereas when G'' is larger than G' the material has a liquid-like behaviour, which means that it flows. The G''/G' ratio is the loss tangent or tan (δ) and gives information on the balance between the viscous and elastic components.

4. Rheological characterisation of ceramic pastes

4.1. Relevant rheological properties of inks for DIW

In the course of a DIW printing process, schematized in Fig. 5, the ink flows initially at a very low speed inside the syringe and undergoes a fast acceleration while being extruded through the nozzle, where a high shear rate is reached. After the deposition of the filament, the ink is once again at rest [116].

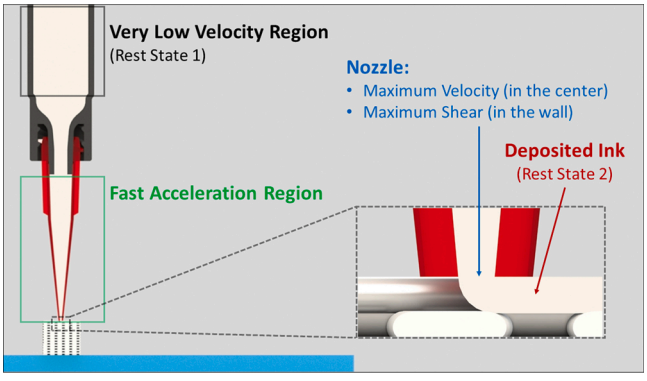

Fig. 5. Schematic diagram of the ink extrusion process through the nozzle in DIW.

In rheological studies it is very important to define the characteristic timescale, mode, and extent of deformation involved in the flow of interest. In the case of DIW, as a first approximation, the extrusion process through a cylindrical nozzle can be modelled by the Hagen–Poiseuille law as a laminar flow of a Newtonian fluid through a pipe [10], which implies a parabolic velocity profile (Eq. (7)) [117]

$$v = 2\bar{v} \cdot \left[1 - \left(\frac{r}{R}\right)^2\right] \tag{7}$$

where $\bar{v}$ represents the average extrusion velocity of the ink (the printing speed) and R the nozzle radius. The velocity equals to zero at the inner wall of the nozzle (r = R) and is maximum at the center (r = 0). Deriving this equation, the shear rate $|\dot{\gamma}|$ is calculated (Eq. (8)), whose maximum value is reached when r = R, *i.e.* in the inner wall of the nozzle (Eq. (9)).

$$|\dot{\gamma}| = \frac{dv}{dr} = 2\bar{v} \cdot \left[\frac{2r}{R^2}\right] \tag{8}$$

$$|\dot{\gamma}|_{max} = \frac{4\bar{v}}{R} \tag{9}$$

As an example, for a printing velocity of 10 mm/s and a nozzle diameter of 250 μm, $|\dot{\gamma}|_{max}$ would be 320 1/s.

The design of a ceramic paste for DIW requires a fine tuning of the rheological properties, which must ensure, on one side, the appropriate flowability of the ink to be extruded through the nozzle and, on another side, a fast recovery of the solid-like behaviour which allows: a) an appropriate shape retention by the extruded filaments and b) a self-supporting capacity by the printed structure. In the following section, after a brief description of the instruments used to characterise the rheological properties of the inks, we will identify the key rheological properties associated to these requirements, and describe the most relevant tests for their characterisation.

4.2. Rotational rheometers

Rotational or shear rheometers are precise instruments able to apply a wide range of shear stresses, shear strains and shear rates to a sample, using specific geometrical configurations and controlling the environmental conditions. The most common configurations are concentric cylinders, cone-plate and parallel plates, where the upper part moves and the lower part is static (Fig. 6).

Specimens can be tested in rotational or oscillatory mode, the latter also known as dynamic testing. In the first one, the upper part rotates in the same direction all the time, whereas in the second one it oscillates sinusoidally with a specific amplitude and frequency. The parallel plate geometry is the most adequate for highly viscous materials, such as the ceramic pastes used for DIW. The gap between plates is variable, although it is recommended to be at least 10 times the size of the biggest particles within the sample.

4.3. Characterisation of the shear-thinning behaviour: Flow sweep test

A desired property for DIW inks is that they have a shear-thinning behaviour, since a decrease of viscosity at increasing shear rate implies a decrease of the extrusion pressure, facilitating smooth extrusion through small nozzles [83,116].

The shear rate dependence of viscosity can be determined by performing a flow sweep, a rotational test that applies an increasing shear rate and measures the evolution of viscosity (Fig. 7a). This test is frequently performed in the rheological characterisation of ceramic pastes for DIW. For an optimal measurement it is recommended to start

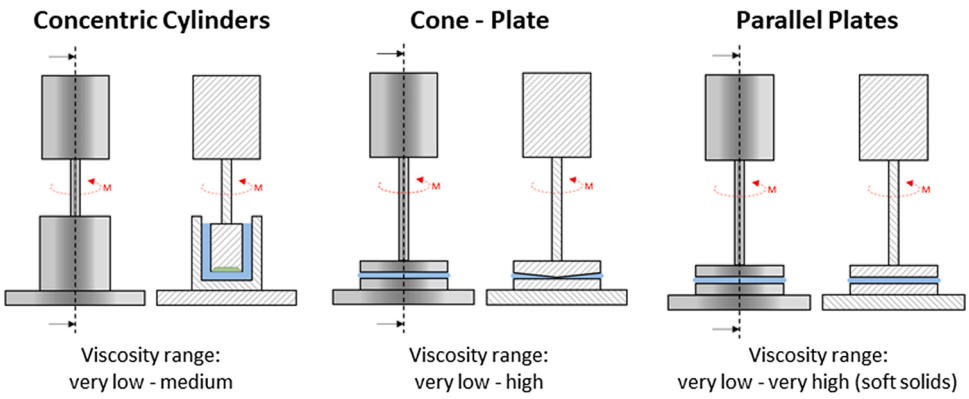

Fig. 6. Rotational rheometer. Schemes of the commercial geometrical configurations.

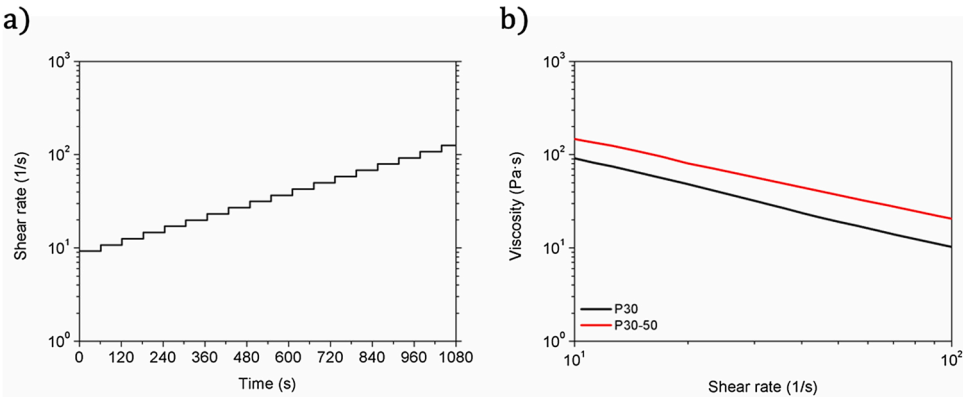

Fig. 7. a) Preset of a flow sweep with 15 points per decade. The shear rate was increased from 5 to 300 1/s stepwise after an equilibrium of the output was reached. b) Outcome of a flow sweep test of a 30 wt.% Pluronic F127 hydrogel and the same hydrogel loaded with 50 wt.% of β-TCP particles, showing a strong shear-thinning behaviour in both cases. Tests carried out at 23 °C, using a 20 mm rough parallel plate geometry with a 500 μm gap and a solvent trap, with a preshearing of 5 1/s for 1 min.

at medium values of shear rate, above the flow point determined in the amplitude sweep test (as described in the next section) to minimize noise, going up until the maximum shear rate experienced by the ceramic paste while being extruded through the nozzle of the 3D printer ($\dot{\gamma}_{max}$), which can be easily estimated by Eq. (9).

Fig. 7b shows the outcomes of a flow sweep test for a 30 wt.% Pluronic F127 hydrogel and the same hydrogel loaded with 50 wt.% of β-tricalcium phosphate (β-TCP) particles. When fitting the Oswald-de Waele Power Law Model (Eq. (2)), values of the flow behaviour index n of 0.042 ± 0.004 and 0.140 ± 0.026 and of the flow consistency parameter k of 837 ± 10 and 1051 ± 60 Pa·s^n are obtained for the hydrogel and the ceramic paste respectively. These results reveal a strong shear-thinning behaviour in both cases, in agreement with previous studies on hydrogel-ceramic DIW inks [29,31,37,40,89,90,97], where n is always smaller than 1. Moreover, in most cases [31,37,40,89,97], the viscosity ranges between 100 and 1000 Pa·s when a shear rate of 10 1/s is applied. Moreover, increasing the ceramic loading has been shown to result in an increase of k, while n is hardly affected [31,40]. Regarding the rheological behaviour of the hydrogel alone, a study about Pluronic hydrogels has shown that an increase of the polymer concentration leads to an increase in the value of k and a decrease in the values of n [118]. A similar behaviour has been reported for organogel binders, although the information is more scarce: n is smaller than 1 in most cases [34,52,56,104,106], an increase in the ceramic loading affects mainly the value of k and a variation on the polymer content modifies both [106]. Overall, these results suggest that the shear-thinning behaviour in this type of inks is associated to the disruption and breakdown of the gel network, which acts as a carrier and governs the rheological properties of the paste above the flow point, and is almost unaffected by the ceramic content of the paste.

In contrast, the shear-thinning behaviour of concentrated colloidal inks is associated to the disruption of interparticle interactions [80]. As a consequence, it is strongly influenced not only by the solid volume fraction [38] and the particles shape and size [119], but also by the ceramic composition [58,76] and surface chemistry, the presence of a dispersant agent [45,65,72], the aging time [39], the pH [62] and the addition of viscosifying additives [38,73].

Once the n index is known, the Rabinowitch expression allows to estimate the shear rate for a non-Newtonian fluid (Eq. (10)) [120]:

$$|\dot{\gamma}|_{non-Newtonian} = \left(\frac{3 + \frac{1}{n}}{4}\right) \cdot |\dot{\gamma}|_{Newtonian} \quad (10)$$

where the bracketed term is the Rabinowitch correction.

4.4. Characterisation of the viscoelastic properties: Amplitude sweep test

The viscoelastic properties are usually characterised by means of oscillatory tests. Specifically, the amplitude sweep test applies a sweep of increasing shear amplitudes at a constant frequency, which implies an increasing shear rate, and measures the evolution of the storage and loss moduli. Fig. 8 shows the outcome of an amplitude sweep of a 30 wt.% Pluronic F127 hydrogel and the same hydrogel loaded with 70 wt.% of β-TCP particles. In both graphs, three zones can be clearly distinguished. In the first one, known as the linear viscoelastic region (LVR), the storage modulus (G') remains constant and is larger than the loss modulus (G"). The shear stress increases linearly with the shear rate, which is associated to a solid-like behaviour with mainly elastic deformation. The value of G' in the LVR is equivalent to the elastic modulus of a solid material and it is known as G'_{eq}. Point 1 is the yield point, and the corresponding yield stress τ_y is the value of the shear stress at the limit of the LVR, where G' starts decreasing, which is associated to the beginning of the break-down of the internal structure, leading to irreversible

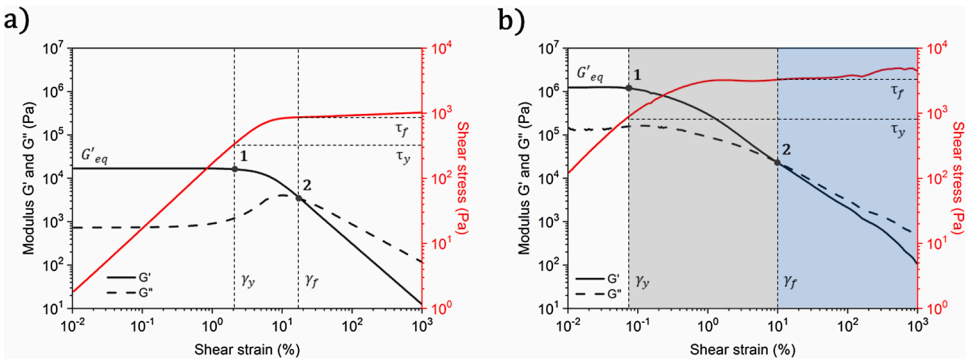

Fig. 8. Amplitude sweep test at a frequency of 1 Hz of a 30 wt.% Pluronic F127 hydrogel (a) and the same hydrogel loaded with 70 wt.% of β-TCP particles (b). Tests carried out at 23 °C, using a 20 mm rough parallel plate geometry with a 500 μm gap and a solvent trap.

deformation. In the second region (grey shaded), between point 1 and point 2, the elastic behaviour still dominates over the viscous (G' > G"), but the yield stress has been overcome, which points to a solid-like behaviour with irreversible deformation. Point 2 is the flow point, when G' equals to G", and represents the transition from solid-like to liquid-like behaviour, which is reached at the flow stress τ_f. After this point, in the flow region (blue shaded), the viscous behaviour dominates over the elastic (G' < G"), which implies the flow of the material due to a progressive breakage and ordering of the internal structure [121].

The effect of loading the hydrogel with ceramic particles (70 wt.%) on the viscoelastic properties is shown in Fig. 8b). The addition of the inorganic powder results in a significant increase of G'_{eq}, as well as a shift of the yield point to smaller shear strains, revealing the major role that the interactions between ceramic particles plays at low shear

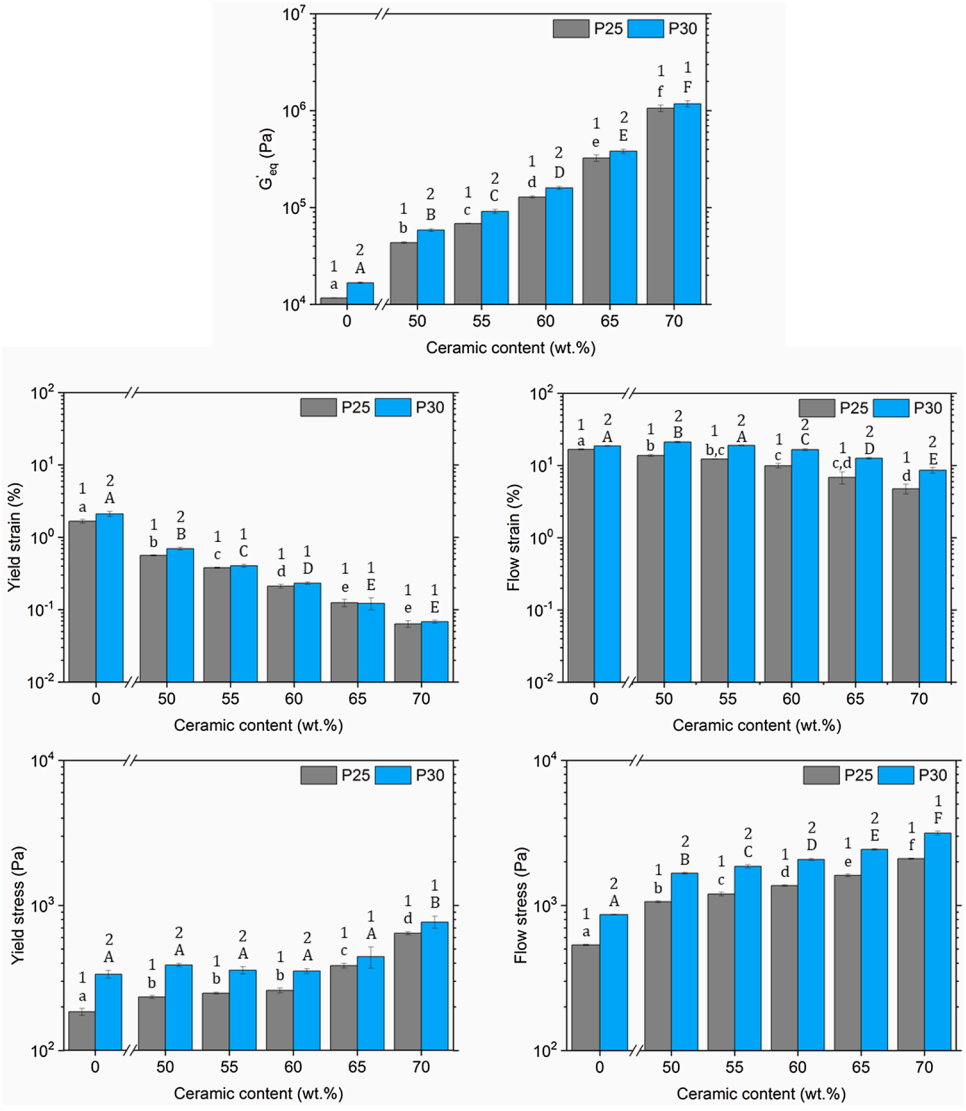

Fig. 9. Effect of the amount of ceramic load and binder concentration on the viscoelastic properties of a β-TCP-Pluronic F127 paste. Data extracted from amplitude sweeps. Bars indicate standard deviation, n=3. Groups identified by the same superscripts are not statistically different (P > 0.05). Letters indicate differences between ceramic loads, in lowercase for the polymer concentration of the binder of 25 wt% and in capital for 30 wt.%, and numbers identify differences between polymer contents in each ceramic load.

strains. This is the case for hydrogel-based inks as well as for colloidal inks [27,119].

Both the amount of ceramic load and the concentration of the hydrogel binder influence the viscoelastic parameters, as shown in Fig. 9, where the viscoelastic properties of pastes with different contents of β-TCP and Pluronic F127 are displayed. On the one hand, G'_{eq} increases significantly with the ceramic content and is otherwise little affected by the hydrogel concentration in the tested range, especially at high ceramic loads. A progressive reduction of the yield strain is also observed with the increase of ceramic content. The hydrogel concentration has no significant effect, except for the hydrogel-only inks and the pastes with the lowest ceramic load. In contrast, the flow strain is less affected by the ceramic fraction, tending to decrease with increasing ceramic content, whereas is more sensitive to the polymer concentration, especially at high ceramic content, increasing with the amount of polymer. Increasing the ceramic load produces an increase in the yield stress when a threshold of 60 or 65 wt.% is exceeded for polymer concentrations of 25 or 30 wt.% respectively. The effect of the polymer concentration is only observed below a 65 wt.% of ceramic and is more pronounced with the reduction of ceramic loading. Lastly, as expected, increasing the ceramic load results also in a gradual increase of the flow stress, which is also increased for higher hydrogel concentrations.

When testing ceramic pastes for DIW, the amplitude sweep test is typically carried out at a frequency of 1 Hz, and it can be performed either controlling the shear strain [37,39,57,84,89,104] or stress [27,38,40,42,44,45,50–52,54,59,73,75,80,122,123]. The strain sweep must cover the relevant range, from very small values such as 0.01 % to values close to the maximum shear rate reached during the DIW process.

To sum up, the amplitude sweep provides crucial information to assess the printability of ceramic pastes, basically: i) the elastic modulus at rest (G'_{eq}); ii) the yield stress, when the material starts to deform plastically (τ_y); and iii) the flow stress, when the material starts to flow (τ_f). Regarding DIW requirements, a high yield stress together with a high elastic modulus minimizes the deformation of the ink once deposited and therefore, prevents the collapsing of the 3D-printed structure. On another hand, a small flow stress minimizes the stress required to force the extrusion of the ink through the nozzle. However, the two parameters are related and therefore a compromise is needed [124].

4.5. Characterisation of the elastic recovery: three interval thixotropy test

Another important aspect that has to be considered in order to achieve self-supporting 3D-structures with good shape fidelity is the transition kinetics from fluid-like flow to solid-like behaviour. A fast recovery is required for the printed paste to retain its shape, since it implies the restoration of the elastic behaviour and avoids the continuous flow of the ink immediately after being extruded as a filament [116]. This can be quantified by measuring the recovery of the shear moduli when there is a drastic decrease of the shear stress from values above the flow point to low, near-rest shear values.

The rheological test that provides this information is the three interval thixotropy test (3ITT), which can be performed either in rotational or oscillatory modes, and allows mimicking an extrusion-based printing process by applying three consecutive steps with different shear rates (Fig. 10a and b): (1) a very small shear rate, within the LVR of the amplitude sweep, that simulates the rest state of the ink while advancing slowly through the 3D printing cartridge; (2) a very high shear rate, above the flow point and as close as possible to $\dot{\gamma}_{max}$, that mimics the extrusion process through the small nozzle; and (3) a very small shear rate again that simulates the rest state of the ink after being deposited. The final goal is to evaluate if the recovery of the solid-like behaviour is fast enough to retain the nozzle shape and if the restored modulus is high enough to ensure a good printing fidelity and the self-supporting capacity of the printed structure. Moreover, the second interval allows to study if the ink's viscosity is time-dependent (thixotropic and rheopectic effects), which would complicate the extrusion process, since the printing parameters, such as printing speed, would need to be continuously adjusted to preserve a constant flow of the material [116].

For the specific case of high laden ceramic pastes, this test or a part of it – the second and third intervals [89] or the last one alone [104] - is rarely performed in rotational mode due to the high shear rate required

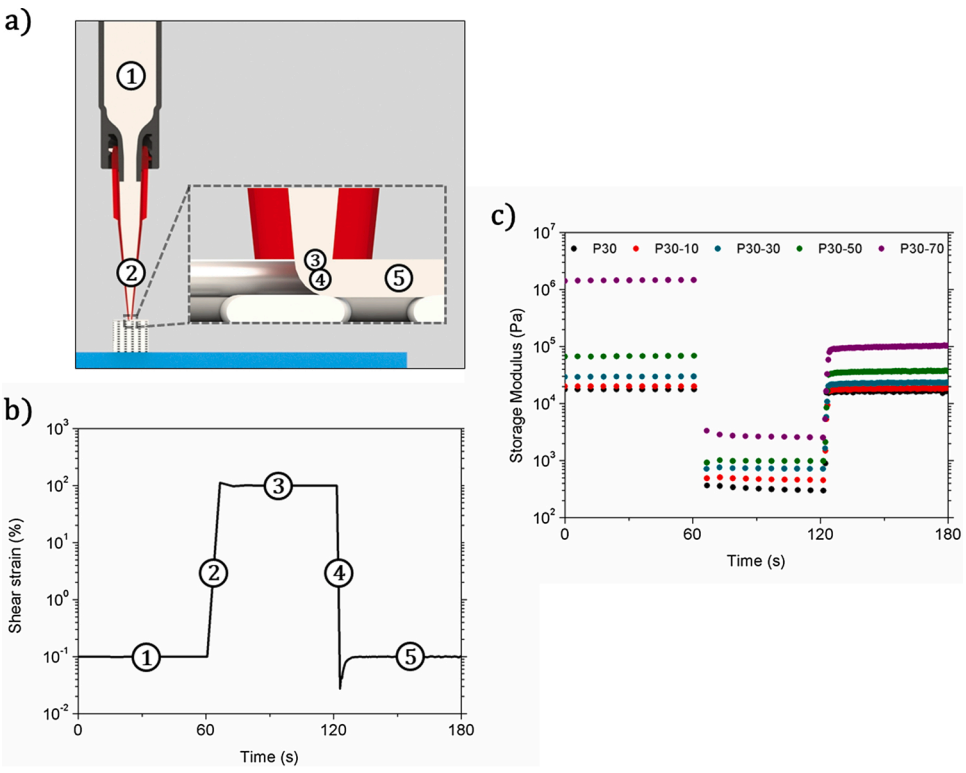

Fig. 10. a) DIW printing process. b) Preset of a 3ITT. The three intervals reproduce the shear rate experienced by the ink during the DIW process, as indicated by the numbers; c) Outcome of a 3ITT of a 30 wt.% Pluronic hydrogel (P30) and the same hydrogel loaded with β-TCP particles: 10 wt. % (P30-10), 30 wt. % (P30-30), 50 wt.% (P30-50) and 70 wt.% (P30-70). Tests performed at a frequency of 1 and at 23 °C, using a 20 mm rough parallel plate geometry with a 500 μm gap and a solvent trap and a fast-sampling data acquisition mode for the third interval.

in the second interval, which can induce slipping problems when testing highly viscous materials. However, a viable alternative is to carry out the test in oscillatory mode, applying a shear strain or stress with constant amplitude and frequency in each step [57,84,90,97,125]. Usually, the frequency is set as 1 Hz as in the amplitude sweep test.

Fig. 10c shows the outcome of a 3ITT of a hydrogel ink with different ceramic contents (0/10/30/50/70 wt.%). In all cases the paste exhibits a solid-like behaviour (G' > G") in the first interval, followed by a fast transition to a liquid-like behaviour (G' < G") that only takes few second in the beginning of the second interval, and subsequently a fast recovery of the solid-like behaviour (G' < G") that also takes few seconds when moving to the third interval. The higher the ceramic content the lower the percentage of the storage modulus from the first interval that is recovered in the third one. Specifically, whereas the 97 % of the storage modulus is recovered in the pristine hydrogel, this value falls to 90 %, 75 %, 52 % and 6 % with ceramic loadings of 10, 30, 50 and 70 wt.%, respectively. Moreover, for the most concentrated pastes (70 $_{wt.}$%) a slight thixotropic effect is observed in the second interval, although the equilibrium is quickly reached. It must be noted that the decrease of storage modulus after extrusion does not necessarily imply that the ink is not adequate for DIW, as long as the final storage modulus is sufficient to retain the shape of the filament and support the printed structure. These results are in accordance with Nan et al., where the same hydrogel was laden with a ≈ 50 wt.% of aluminum particles [57]. In contrast, a complete recovery was achieved by Diloksumpan et al. when a 40 wt/v % Pluronic hydrogel was laden with 70 wt. % of CaP particles [97]. In the same line, 6 wt.% Polyvinyl alcohol hydrogel laden with 57.52 wt.% of silicon nitride particles resulted in a full recovery in few seconds [90].

For colloidal pastes, Nan et al. proved that a small amount of polyethyleneimine (PEI) in a ≈ 76 wt.% suspension of titania increased significantly the storage modulus due to the flocculating effect of the cationic additive and induced a fast and complete elastic recovery owing to the electrostatic anionic-cationic interactions occurring in the ink. This fast and complete elastic recovery was a key feature in order to be able to 3D print free-standing pillars. Moreover, both the storage modulus and the elastic recovery was shown to be highly dependent on the concentration of PEI [57]. On the other hand, Chen et al. tested magnesium phosphate gels with thixotropic properties based on electrostatic interactions, showing that the solid-like behaviour of the inks was recovered immediately but there was a progressive increase of the storage modulus with time until reaching the original value [84].

4.6. Characterisation of the temperature dependence of viscoelastic properties: temperature Ramp

Viscosity varies strongly with temperature because it is closely linked to molecular motion. Moreover, some materials experience temperature-dependent transitions resulting in drastic changes in viscosity, associated for instance to gelling processes or glass transitions in polymers. This is the case of some hydrogels commonly used as binders for ceramic inks, which undergo a reversible gelation process at a certain temperature. For example, Pluronic F127, a commercially available linear ABA triblock copolymer with A being poly(ethylene oxide) (PEO) and B poly(propylene oxide) (PPO). Below the gelation temperature, water is a good solvent for both PEO and PPO, but as the temperature increases, the hydrophobicity of the PPO increases and its solubility decreases, leading to the formation PPO-PEO core-shell micelles. At low concentrations these micelles are physically separated and do not interact, but above a certain concentration they organize themselves into a lattice and form a gel [126].

The temperature dependence of the rheological properties is usually characterised by performing a temperature ramp, either in rotational or in oscillatory mode. In most cases, the direction of the ramp affects the results.

In rotational mode, the most typically used in hydrogels [118], the sample is rotated at a small and constant shear rate while simultaneously increasing or decreasing the temperature, and the evolution of viscosity is recorded. In contrast, in the oscillatory mode, an oscillating shear strain with a small and constant amplitude and a constant frequency is applied, within the LVR, and the evolution of the storage and loss moduli is measured [127]. For an optimal measurement it is recommended to use the smallest possible gap and a temperature ramp rate between 1 and 5 °C/min to minimize temperature gradients within the sample. This test provides a good understanding of the dependence of the rheological properties of the ink on temperature, and allows determining the optimal printing temperature.

Fig. 11 illustrates the information provided by a temperature ramp either in rotational or in oscillatory mode, for a 30 wt.% Pluronic F127 hydrogel and for the same hydrogel loaded with 65 wt.% β -TCP particles. The hydrogel undergoes a drastic increase of the viscosity/modulus around 10 °C, that is the gelling temperature. Below this temperature it behaves as a fluid (G''>G') and above it has a solid-like behaviour (G'>G'') (Fig. 11b). This transformation is also visible in the ceramic suspension, but less markedly due to the presence of the ceramic particles that mitigate the phenomenon. Moreover, whereas the gelation process induces a liquid-like to solid-like transition in the hydrogel, the ceramic paste has a solid-like behaviour over the whole range of temperatures. Therefore, this ink should be printed above this temperature in order to take advantage of the viscoelastic properties of the hydrogel at low shear rates, in order to maximize the shape-retention ability and self-supporting capacity.

This test provides essential information about the gelling process of DIW inks when thermosensitive binders, such as Pluronic, are used, as reported for instance for ceria-stabilized zirconia or alumina inks [37,40].

5. Rheological properties as printability predictors

Although the concept of good or poor printability seems rather intuitive and has been extensively used in the 3D-printing literature, there is a lack of consensus about the appropriate methodology to assess the printability of an ink [128]. In DIW the term printability encompasses two different concepts, namely: i) suitable extrudability; and ii) good shape-fidelity, both of the individual filaments and of the 3D-printed structure, also referred to as printing accuracy [116]. Both concepts are directly related to the rheological properties of the ink.

Some rheological parameters can be considered as key predictors of printability aspects, as displayed in Table 3, and can be divided in two main groups:

The first group is linked to the extrudability of an ink, and is composed by the flow stress (τ_f) and the flow behaviour index (n). The first parameter represents the minimum shear stress required to make the ink flow, which is related to the minimum force required by the 3D-printer to extrude an ink, and the second one describes the flow behaviour of the material. A shear-thinning behaviour is desired, as it implies a smaller extrusion pressure at the same extrusion speed than a Newtonian or a shear-thickening material, and in fact printable ceramic inks have been shown to have n<1, although a wide range of values has been reported (0.04−0.94). Values of τ_f between 25 Pa and 5 kPa, although most of them in the range of 0.1–2 kPa have been reported.

The second group is related to shape fidelity. It is important to note that, unlike when using polymeric materials, printing is not the final step when manufacturing ceramic parts by DIW. Most ceramic inks require post-printing treatments, which involve shrinkage, very significant in the case of sintering and minor in the case of reactive inks that harden by chemical bonding processes. These dimensional changes must be taken into account when designing the CAD model of the green parts, and the shape fidelity of the green part is a crucial aspect to ensure the accuracy of the whole process. To achieve it the paste must withstand both the gravitational forces and the surface tension after being extruded, as well as the shear stresses induced by printing the consecutive layers. This applies both to the individual filaments, which must retain the shape of

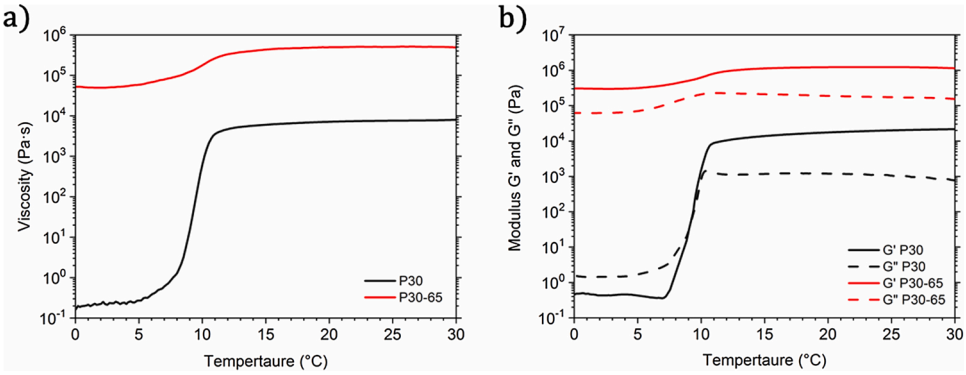

Fig. 11. Temperature ramps of 30 wt.% Pluronic F127 hydrogel and the same hydrogel loaded with a 65 wt.% of β-TCP particles performed by decreasing the temperature from 30 °C to 0 °C with a ramp rate of 1 °C/min, using a 20 mm rough parallel plate geometry with a 500 μm gap and a solvent trap. a) Applying a shear rate of 0.1 and 0.01 1/s for the hydrogel alone and loaded in rotational mode. b) Applying a shear strain of 0.1 % for both materials in oscillatory mode with a frequency of 1 Hz.

Table 3
Rheological parameters as key predictors of printability aspects, and measured values for different ceramic inks.

Predictor of	Rheological parameter		Significance	Values from ceramic inks	Ref.
Extrudability	Flow stress τ_f		The minimum shear stress required to make the ink flow	25–50 Pa	[27,79]
				100–200 Pa	[38,42,50,71,104]
				200–300 Pa	[54,83,89,104]
				300–500 Pa	[42,45,54,71]
				500–800 Pa	[38,40,51,54]
				1–2 KPa	[40,44,52,54,73,106]
				5 KPa	[59]
	Flow Behaviour Index n		Describes the flow behaviour	0.04–0.05	[73]
				0.1–0.2	[40,83]
				0.3–0.5	[34,39,42,45,50,59]
				0.64–0.73	[27,35,41,89]
				0.89–0.94	[44,106]
				Not specified but shear-thinning behaviour (n<1)	[31,37,38,52,56,58,65,71,72,76,84,90,97,104]
Shape fidelity	Storage Modulus at rest G'_{eq}		Stiffness of the ink at rest	1KPa	[45]
				2–10 KPa	[39,44,54,104]
				25–200 KPa	[27,38,40,42,50,59,71,79,83,84,89,90,106]
				200–700 KPa	[38,51,52,73,106]
				1000–3000 KPa	[38,40,107]
				4000–10000 KPa	[37,57]
	Damping factor G''/G' at rest		Relation between the solid and liquid behaviour at rest	0.1–0.3	[39]
	Yield Stress τ_y		Maximum stress that the ink can support without suffering irreversible deformation	10–70 Pa	[34,38,50,79]
				100–200 Pa	[34,38,41,44,45,71]
				200–300 Pa	[71]
				300–800 Pa	[38–40,51,52,73,106]
				1–1.5 KPa	[40,59,107]
	Elastic Recovery	Time	Time required to recover the elastic behaviour just immediately after being extruded	Few seconds	[57,84]
		Percentage	Percentage of G'_{eq} obtained in the elastic recovery	30 % after few seconds	[57]
				100 % after 330 s	
				≈ 3 % after few seconds	[84]
				92 % after 30 min.	

the nozzle and not sag, and to the whole structure, which must be able to support layer stacking without deformation. The relevant parameters are the storage modulus at rest (G'_{eq}), the damping factor (G''/G') and the yield stress (τ_y). G'_{eq} represents the elastic modulus of a solid material and, therefore, is linked to the stiffness at rest. Values from 1 to 10,000 kPa were reported for pintable ceramic inks, mostly in the range from 25 to 200 kPa. The damping factor allows to quickly screen the dominant behaviour of the ink at rest, either elastic (G''/G' <1) or

viscous (G''/G'>1). However, it has hardly ever been used in the DIW ceramic literature and only values between 0.1 and 0.3 for printable inks were reported by M'Barki et al. [39]. τ_y represents the maximum stress a material can support without suffering irreversible deformation and values between 10 Pa and 1.5 kPa were reported for printable ceramic inks, most commonly between 100 and 800 Pa.

In this respect, Minas et al., based on their experimental data from emulsion inks, defined as a printability criterion for ceramic inks to meet the following conditions: $G'_{eq} > 2$ kPa, and $\tau_y > 200\ Pa$ (although it has to be noted that their definition of τ_y corresponds to τ_f in the present work) [54]. Although most of the printable ceramic pastes meet this criterion (Table 3), there are some exceptions. Thus, a boron carbide colloidal ink was reported to have G'_{eq} around 1 kPa [45]. Other ink formulations were reported to have slightly smaller τ_f, between 100 and 200 Pa [38,42,50,71,104] and there are also two cases of colloidal suspensions with significantly smaller τ_f, in the range of 25−50 Pa [27,79].

The characterisation of the thixotropy of the inks is also a relevant aspect that gives information on shape fidelity. This can be done through the three interval thixotropy test (3ITT). A fast recovery of the elastic properties just immediately after being extruded would ensure the retention of the nozzle shape by the filament. Although this has been little explored as a method to predict printability, Nan et al. [57] showed a direct relation between the kinetics of the elastic recovery and the capacity of the ink to retain its shape in very demanding conditions, e.g. when printing vertical pillars. Both the time required to recover the elastic behaviour and the percentage of the original value of G'_{eq} recovered after deformation are relevant parameters provided by this test [57].

However, it is important to bear in mind that shape fidelity, besides depending on the rheological properties of the ink, also depends on the design of the part and the printing parameters. In this context, Smay et al. [27] defined the minimum G'_{eq} required for printing spanning structures with a maximum deflection of 5 % of the nozzle diameter, taking into account the gravitational forces that have to be counteracted in order to prevent filament sagging (Eq. (12)) [27]

$$G'_{eq} \geq 1.4\gamma s^4 D \tag{12}$$

where γ is the specific weight of the ink, D the nozzle diameter and s the reduced span distance ($= L/D$).

Another criterion was suggested by Barki et al. [39], taking into account the surface tension in addition to the gravitational forces. Thus, the post-extruded yield stress (known as dynamic yield stress τ_y^{Dyn}) must be equal to or higher than the forces of gravity (ρgh) and surface tension ($\gamma_s R^{-1}$). Therefore, the figure of merit Ξ should be equal or higher than 1 (Eq. (13)) [39]

$$\Xi = \frac{\tau_y^{Dyn}}{\rho g h + \gamma_s R^{-1}} \tag{13}$$

Where ρ is the density of the paste, h the height of the part, γ_s the surface tension and R the radius of curvature of the smallest printed feature, in most cases the radius of a single filament.

Alternatively, Feilden [129] defined a paste specific figure of merit $\varnothing$ (Eq. (14) [129]), based on minimizing the lateral deflection of the printed part as a result of the force that the nozzle imparts when the ink is deposited (Fig. 12a).

$$\varnothing = \frac{G'_{eq}}{\tau_f} \tag{14}$$

The higher the value of $\varnothing$, the less the part is expected to deform due to the stresses it is subjected to during the printing process itself. There are some additional requirements for the yield stress, such as the need of a minimum yield stress to allow the part of a set height to be self-supporting, and a maximum value that is dependent on the force that the printer can apply. This can be visualized by plotting G'_{eq} vs τ_f, as shown in Fig. 12b for different pastes compiled from the literature, showing that most of those declared printable by the respective authors had $\varnothing$ values greater than 20 [129].

Finally, it is worth mentioning that different methods, complementary to the rheological characterisation, have been proposed to assess the printability of inks, based on shape fidelity. Most of them rely on visual inspection or image analysis, and are aimed at verifying the degree of dimensional accuracy of the printed object compared to the designed model. Its use is widespread in the bioprinting field, where hydrogel-based inks are typically used, but the concepts are valid also for ceramic-based inks. The focus can be either on the individual filaments or on the 3D-printed parts as a whole. Regarding single filaments, some relevant aspects include: (1) their geometry before and after being deposited on the previous layer, which should be continuous and uniform, with filament section close to the nozzle shape [116]; (2) filament sagging, that can be quantified by printing a single filament over a row of pillars separated by increasing distances and measuring the maximum deflection in the centre of each gap [130]; and (3) filament fusion, determined by printing parallel filaments with a stepwise widening of the spacing between them [130]. Some fusion is required to ensure adhesion between layers but too much may reduce shape-fidelity. Regarding 3D-printed structures as a whole, the final goal is to assess the geometrical deviation of the printed structure with respect to the computer design or a control [131–135], which can be quantified by the Shape Fidelity Scale [136] or the Pore Factor [133,134,137–139].

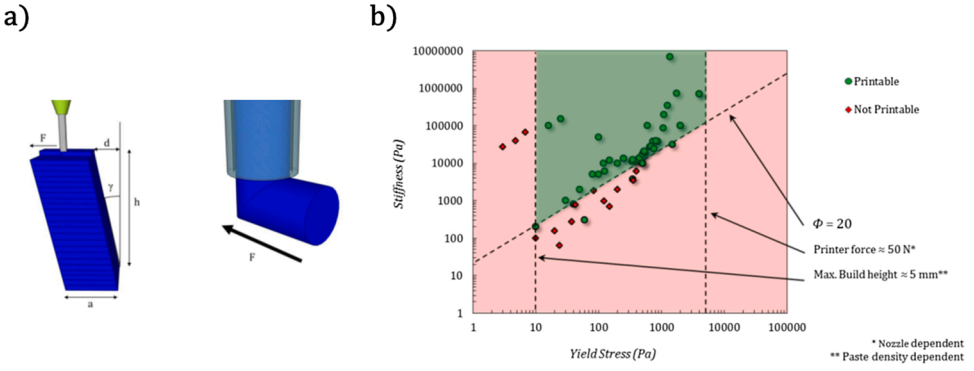

Fig. 12. Feilden's figure of merit to predict printability: a) tilting of a high aspect ratio part due to the force exerted on it when printing subsequent filaments; b) Plot of G'_{eq} against τ_y (τ_f in this work) for different ceramic pastes from the literature, compiled by Feilden and classified in terms of the declared printability and the figure of merit $\varnothing$. From Ref. [129].

6. Conclusions and outlook

A wide range of ceramic pastes have been developed so far as inks for microextrusion based 3D-printing to manufacture ceramic parts with complex geometries. The first generation of inks consisted mainly in highly loaded colloidal suspensions in a low-viscosity liquid, usually water, with a viscoelastic behaviour derived from the interparticle interactions, which are very sensitive to variations on the chemistry and pH of the environment. In recent years the liquid phase has been replaced by hydrogels or organogels, achieving more robust viscoelastic properties.

The DIW process imposes stringent requirements on the ink's rheological behaviour. Moreover, as applications become more sophisticated, such as 4D printing or patient personalized products, a more accurate control of the geometry is required. Hence the increasing demand for inks with excellent printability, which encompasses extrudability and shape fidelity. Often the development of ink formulations has been based on trial-and-error processes, which is highly inefficient and time-consuming, and has overlooked the rheological characterisation. A thorough characterisation of the key rheological parameters may provide very relevant information to understand the effect of different factors on printability and to address a rational design of ink formulations with better performance.

Declaration of Competing Interest

The authors report no declarations of interest.

Acknowledgements

The authors acknowledge the Spanish Ministry of Science and Innovation for financial support through the PID2019-103892RB-I00/AEI/10.13039/501100011033 project and the FPU scholarship of LdMB. They also thank the Generalitat the Catalunya for funding through projects 2017SGR-1165 and BASE3D 001-P-001646, co-funded by European Regional Development Funds, as well as the ICREA Academia award of MPG.

References

[1] M. Bhuvanesh Kumar, P. Sathiya, Methods and materials for additive manufacturing: a critical review on advancements and challenges, Thin-Walled Struct. 159 (October 2020) (2021) 107228, https://doi.org/10.1016/j.tws.2020.107228.
[2] S.C. Ligon, R. Liska, J. Stampfl, M. Gurr, R. Mülhaupt, Polymers for 3D printing and customized additive manufacturing, Chem. Rev. 117 (15) (2017) 10212–10290, https://doi.org/10.1021/acs.chemrev.7b00074.
[3] S.S. Alghamdi, S. John, N.R. Choudhury, N.K. Dutta, Additive manufacturing of polymer materials: progress, promise and challenges, Polymers 13 (5) (2021) 753, https://doi.org/10.3390/polym13050753.
[4] M.B.A. Tamez, I. Taha, A review of additive manufacturing technologies and markets for thermosetting resins and their potential for carbon fiber integration, Addit. Manuf. 37 (October 2020) (2021) 101748, https://doi.org/10.1016/j.addma.2020.101748.
[5] D. Herzog, V. Seyda, E. Wycisk, C. Emmelmann, Additive manufacturing of metals, Acta Mater. 117 (2016) 371–392, https://doi.org/10.1016/j.actamat.2016.07.019.
[6] A. Vafadar, F. Guzzomi, A. Rassau, K. Hayward, Advances in metal additive manufacturing: a review of common processes, industrial applications, and current challenges, Appl. Sci. 11 (3) (2021) 1–33, https://doi.org/10.3390/app11031213.
[7] E. Peng, D. Zhang, J. Ding, Ceramic robocasting: recent achievements, potential, and future developments, Adv. Mater. 30 (47) (2018), 1802404, https://doi.org/10.1002/adma.201802404.
[8] N. Travitzky, et al., Additive manufacturing of ceramic-based materials, Adv. Eng. Mater. 16 (6) (2014) 729–754, https://doi.org/10.1002/adem.201400097.
[9] R. Trombetta, J.A. Inzana, E.M. Schwarz, S.L. Kates, H.A. Awad, 3D printing of calcium phosphate ceramics for bone tissue engineering and drug delivery, Ann. Biomed. Eng. 45 (1) (2017) 23–44, https://doi.org/10.1007/s10439-016-1678-3.
[10] E.N. Udofia, W. Zhou, Microextrusion based 3D printing – a review, in: Proc. 29th Annu. Int. Solid Free. Fabr. Symp. – An Addit. Manuf. Conf., August, 2018, pp. 2033–2060.
[11] F. Bos, R. Wolfs, Z. Ahmed, T. Salet, Additive manufacturing of concrete in construction: potentials and challenges of 3D concrete printing, Virtual Phys. Prototyp. 11 (3) (2016) 209–225, https://doi.org/10.1080/17452759.2016.1209867.
[12] A. Paolini, S. Kollmannsberger, E. Rank, Additive manufacturing in construction: a review on processes, applications, and digital planning methods, Addit. Manuf. 30 (September) (2019) 100894, https://doi.org/10.1016/j.addma.2019.100894.
[13] Y. Maazouz, et al., Robocasting of biomimetic hydroxyapatite scaffolds using self-setting inks, J. Mater. Chem. B 2 (33) (2014) 5378–5386, https://doi.org/10.1039/c4tb00438h.
[14] S. Raymond, et al., Accelerated hardening of nanotextured 3D-plotted self-setting calcium phosphate inks, Acta Biomater. 75 (2018) 451–462, https://doi.org/10.1016/j.actbio.2018.05.042.
[15] Y. Maazouz, E.B. Montufar, J. Malbert, M. Espanol, M.P. Ginebra, Self-hardening and thermoresponsive alpha tricalcium phosphate/pluronic pastes, Acta Biomater. 49 (2017) 563–574, https://doi.org/10.1016/j.actbio.2016.11.043.
[16] H. Shao, et al., 3D robocasting magnesium-doped wollastonite/TCP bioceramic scaffolds with improved bone regeneration capacity in critical sized calvarial defects, J. Mater. Chem. B 5 (16) (2017) 2941–2951, https://doi.org/10.1039/c7tb00217c.
[17] S.M. Bittner, et al., Fabrication and mechanical characterization of 3D printed vertical uniform and gradient scaffolds for bone and osteochondral tissue engineering, Acta Biomater. 90 (2019) 37–48, https://doi.org/10.1016/j.actbio.2019.03.041.
[18] T. Almela, et al., Simulation of cortico-cancellous bone structure by 3D printing of bilayer calcium phosphate-based scaffolds, Bioprinting 6 (April) (2017) 1–7, https://doi.org/10.1016/j.bprint.2017.04.001.
[19] P. Miranda, E. Saiz, K. Gryn, A.P. Tomsia, Sintering and robocasting of β-tricalcium phosphate scaffolds for orthopaedic applications, Acta Biomater. 2 (4) (2006) 457–466, https://doi.org/10.1016/j.actbio.2006.02.004.
[20] S. Michna, W. Wu, J.A. Lewis, Concentrated hydroxyapatite inks for direct-write assembly of 3-D periodic scaffolds, Biomaterials 26 (28) (2005) 5632–5639, https://doi.org/10.1016/j.biomaterials.2005.02.040.
[21] J. Franco, P. Hunger, M.E. Launey, A.P. Tomsia, E. Saiz, Direct write assembly of calcium phosphate scaffolds using a water-based hydrogel, Acta Biomater. 6 (1) (2010) 218–228, https://doi.org/10.1016/j.actbio.2009.06.031.
[22] I.H. Jo, M.K. Ahn, Y.W. Moon, Y.H. Koh, H.E. Kim, Novel rapid direct deposition of ceramic paste for porous biphasic calcium phosphate (BCP) scaffolds with tightly controlled 3-D macrochannels, Ceram. Int. 40 (7 PART B) (2014) 11079–11084, https://doi.org/10.1016/j.ceramint.2014.03.125.
[23] J.L. Simon, et al., In vivo bone response to 3D periodic hydroxyapatite scaffolds assembled by direct ink writing, J. Biomed. Mater. Res. Part A 83A (December (3)) (2007) 747–758, https://doi.org/10.1002/jbm.a.31329.
[24] B. Huang, G. Caetano, C. Vyas, J.J. Blaker, C. Diver, P. Bártolo, Polymer-ceramic composite scaffolds: the effect of hydroxyapatite and β-tri-calcium phosphate, Materials (Basel) 11 (January (1)) (2018) 129, https://doi.org/10.3390/ma11010129.
[25] A.E. Jakus, et al., Hyperelastic 'bone': a highly versatile, growth factor-free, osteoregenerative, scalable, and surgically friendly biomaterial, Sci. Transl. Med. 8 (358) (2016) 1–16, https://doi.org/10.1126/scitranslmed.aaf7704.
[26] A.R. Akkineni, Y. Luo, M. Schumacher, B. Nies, A. Lode, M. Gelinsky, 3D plotting of growth factor loaded calcium phosphate cement scaffolds, Acta Biomater. 27 (2015) 264–274, https://doi.org/10.1016/j.actbio.2015.08.036.
[27] J.E. Smay, J. Cesarano, J.A. Lewis, Colloidal inks for directed assembly of 3-D periodic structures, Langmuir 18 (14) (2002) 5429–5437, https://doi.org/10.1021/la0257135.
[28] C.F. Marques, et al., Biphasic calcium phosphate scaffolds fabricated by direct write assembly: mechanical, anti-microbial and osteoblastic properties, J. Eur. Ceram. Soc. 37 (1) (2017) 359–368, https://doi.org/10.1016/j.jeurceramsoc.2016.08.018.
[29] Q. Fu, E. Saiz, A.P. Tomsia, Direct ink writing of highly porous and strong glass scaffolds for load-bearing bone defects repair and regeneration, Acta Biomater. 7 (10) (2011) 3547–3554, https://doi.org/10.1016/j.actbio.2011.06.030.
[30] H. Elsayed, P. Colombo, E. Bernardo, Direct ink writing of wollastonite-diopside glass-ceramic scaffolds from a silicone resin and engineered fillers, J. Eur. Ceram. Soc. 37 (13) (2017) 4187–4195, https://doi.org/10.1016/j.jeurceramsoc.2017.05.021.
[31] A. Nommeots-Nomm, P.D. Lee, J.R. Jones, Direct ink writing of highly bioactive glasses, J. Eur. Ceram. Soc. 38 (3) (2018) 837–844, https://doi.org/10.1016/j.jeurceramsoc.2017.08.006.
[32] H. Elsayed, M. Picicco, A. Dasan, J. Kraxner, D. Galusek, E. Bernardo, Glass powders and reactive silicone binder: interactions and application to additive manufacturing of bioactive glass-ceramic scaffolds, Ceram. Int. 45 (11) (2019) 13740–13746, https://doi.org/10.1016/j.ceramint.2019.04.070.
[33] Q. Fu, E. Saiz, A.P. Tomsia, Bioinspired strong and highly porous glass scaffolds, Adv. Funct. Mater. 21 (6) (2011) 1058–1063, https://doi.org/10.1002/adfm.201002030.
[34] A.M. Deliormanli, M.N. Rahaman, Direct-write assembly of silicate and borate bioactive glass scaffolds for bone repair, J. Eur. Ceram. Soc. 32 (14) (2012) 3637–3646, https://doi.org/10.1016/j.jeurceramsoc.2012.05.005.
[35] S. Eqtesadi, A. Motealleh, P. Miranda, A. Pajares, A. Lemos, J.M.F. Ferreira, Robocasting of 45S5 bioactive glass scaffolds for bone tissue engineering, J. Eur. Ceram. Soc. 34 (1) (2014) 107–118, https://doi.org/10.1016/j.jeurceramsoc.2013.08.003.
[36] J. Barberi, et al., Robocasting of SiO2-based bioactive glass scaffolds with porosity gradient for bone regeneration and potential load-bearing applications, Materials (Basel). 12 (7) (2019), 2691, https://doi.org/10.3390/ma12172691.

[37] L. Goyos-Ball, et al., Mechanical and biological evaluation of 3D printed 10CeTZP-Al2O3 structures, J. Eur. Ceram. Soc. 37 (9) (2017) 3151–3158, https://doi.org/10.1016/j.jeurceramsoc.2017.03.012.
[38] T. Chen, et al., Rheological behavior of titania ink and mechanical properties of titania ceramic structures by 3D direct ink writing using high solid loading titania ceramic ink, J. Alloys Compd. 783 (2019) 321–328, https://doi.org/10.1016/j.jallcom.2018.12.334.
[39] A. M'Barki, L. Bocquet, A. Stevenson, Linking rheology and printability for dense and strong ceramics by direct ink writing, Sci. Rep. 7 (2017), 6017, https://doi.org/10.1038/s41598-017-06115-0.
[40] E. Feilden, E.G.T. Blanca, F. Giuliani, E. Saiz, L. Vandeperre, Robocasting of structural ceramic parts with hydrogel inks, J. Eur. Ceram. Soc. 36 (10) (2016) 2525–2533, https://doi.org/10.1016/j.jeurceramsoc.2016.03.001.
[41] L. Rueschhoff, W. Costakis, M. Michie, J. Youngblood, R. Trice, Additive manufacturing of dense ceramic parts via direct ink writing of aqueous alumina suspensions, Int. J. Appl. Ceram. Technol. 13 (5) (2016) 821–830, https://doi.org/10.1111/ijac.12557.
[42] E. Peng, et al., Robocasting of dense yttria-stabilized zirconia structures, J. Mater. Sci. 53 (1) (2018) 247–273, https://doi.org/10.1007/s10853-017-1491-x.
[43] C.F. Revelo, H.A. Colorado, 3D printing of kaolinite clay ceramics using the Direct Ink Writing (DIW) technique, Ceram. Int. 44 (5) (2018) 5673–5682, https://doi.org/10.1016/j.ceramint.2017.12.219.
[44] Q. Sun, Z. Yang, H. Cheng, Y. Peng, Y. Huang, M. Chen, Creation of three-dimensional structures by direct ink writing with kaolin suspensions, J. Mater. Chem. C 6 (42) (2018) 11392–11400, https://doi.org/10.1039/c8tc03152e.
[45] W.J. Costakis, L.M. Rueschhoff, A.I. Diaz-Cano, J.P. Youngblood, R.W. Trice, Additive manufacturing of boron carbide via continuous filament direct ink writing of aqueous ceramic suspensions, J. Eur. Ceram. Soc. 36 (14) (2016) 3249–3256, https://doi.org/10.1016/j.jeurceramsoc.2016.06.002.
[46] B. Chen, Y. Jiang, X. Tang, Y. Pan, S. Hu, Fully packaged carbon nanotube supercapacitors by direct ink writing on flexible substrates, ACS Appl. Mater. Interfaces 9 (34) (2017) 28433–28440, https://doi.org/10.1021/acsami.7b06804.
[47] M. Wei, F. Zhang, W. Wang, P. Alexandridis, C. Zhou, G. Wu, 3D direct writing fabrication of electrodes for electrochemical storage devices, J. Power Sources 354 (2017) 134–147, https://doi.org/10.1016/j.jpowsour.2017.04.042.
[48] Y. Zhang, et al., Recent progress of direct ink writing of electronic components for advanced wearable devices, ACS Appl. Electron. Mater. 1 (9) (2019) 1718–1734, https://doi.org/10.1021/acsaelm.9b00428.
[49] J.E. Smay, B. Tuttle, J.C. Iii, Robocasting of three-dimensional piezoelectric structures. Piezoelectric Acoust. Mater. Transducer Appl., 2008, pp. 305–318, https://doi.org/10.1007/978-0-387-76540-2_15.
[50] Y.Y. Li, L.T. Li, B. Li, Direct ink writing of 3-3 piezoelectric composite, J. Alloys Compd. 620 (2015) 125–128, https://doi.org/10.1016/j.jallcom.2014.09.124.
[51] Y. Li, B. Li, J. Sun, K. Cai, J. Zhou, L. Li, Direct write assembly of 3-dimensional structures with aqueous-based piezoelectric inks, Key Eng. Mater. 512–515 (2012) 390–394, https://doi.org/10.4028/www.scientific.net/KEM.512-515.390.
[52] C.M. Larson, et al., Direct ink writing of silicon carbide for microwave optics, Adv. Eng. Mater. 18 (1) (2016) 39–45, https://doi.org/10.1002/adem.201500298.
[53] T.A. Baer, J. Cesarano III, P. Calvert, J. Cesarano, T.A. Baer, P. Calvert, Recent developments in freeform fabrication of dense ceramics from slurry deposition, Solid Free. Fabr. Proceedings (1997) 25–32. September 1997.
[54] C. Minas, D. Carnelli, E. Tervoort, A.R. Studart, 3D printing of emulsions and foams into hierarchical porous ceramics, Adv. Mater. 28 (45) (2016) 9993–9999, https://doi.org/10.1002/adma.201603390.
[55] N. Golafshan, et al., Tough magnesium phosphate-based 3D-printed implants induce bone regeneration in an equine defect model, Biomaterials 261 (2020) 120302, https://doi.org/10.1016/j.biomaterials.2020.120302.
[56] X. Lu, Y. Lee, S. Yang, Y. Hao, J.R.G. Evans, C.G. Parini, Solvent-based paste extrusion solid freeforming, J. Eur. Ceram. Soc. 30 (1) (2010) 1–10, https://doi.org/10.1016/j.jeurceramsoc.2009.07.019.
[57] B. Nan, F.J. Galindo-Rosales, J.M.F. Ferreira, 3D printing vertically: direct ink writing free-standing pillar arrays, Mater. Today 35 (May) (2020) 16–24, https://doi.org/10.1016/j.mattod.2020.01.003.
[58] Q. Sun, et al., Fabrication of 3D structures via direct ink writing of kaolin/graphene oxide composite suspensions at ambient temperature, Ceram. Int. 45 (15) (2019) 18972–18979, https://doi.org/10.1016/j.ceramint.2019.06.136.
[59] Q. Sun, et al., Direct ink writing of 3D cavities for direct plated copper ceramic substrates with kaolin suspensions, Ceram. Int. 45 (9) (2019) 12535–12543, https://doi.org/10.1016/j.ceramint.2019.03.191.
[60] E. Ordoñez, J.M. Gallego, H.A. Colorado, 3D printing via the direct ink writing technique of ceramic pastes from typical formulations used in traditional ceramics industry, Appl. Clay Sci. 182 (53) (2019) 105285, https://doi.org/10.1016/j.clay.2019.105285.
[61] J. Cesarano, et al., Customization of load-bearing hydroxyapatite lattice scaffolds, Int. J. Appl. Ceram. Technol. 2 (May (3)) (2005) 212–220, https://doi.org/10.1111/j.1744-7402.2005.02026.x.
[62] J.N. Stuecker, J. Cesarano, D.A. Hirschfeld, Control of the viscous behavior of highly concentrated mullite suspensions for robocasting, J. Mater. Process. Technol. 142 (2) (2003) 318–325, https://doi.org/10.1016/S0924-0136(03)00586-7.
[63] B.A. Tuttle, et al., Robocast Pb(Zr 0.95 Ti 0.05)O 3 ceramic monoliths and composites, J. Am. Ceram. Soc. 84 (4) (2001) 872–874, https://doi.org/10.1111/j.1151-2916.2001.tb00756.x.
[64] J.E. Smay, J. Cesarano, B.A. Tuttle, J.A. Lewis, Piezoelectric properties of 3-X periodic Pb(Zr xTi 1-x)O 3-polymer composites, J. Appl. Phys. 92 (10) (2002) 6119–6127, https://doi.org/10.1063/1.1513202.
[65] S. Zhao, W. Xiao, M.N. Rahaman, D. O'Brien, J.W. Seitz-Sampson, B. Sonny Bal, Robocasting of silicon nitride with controllable shape and architecture for biomedical applications, Int. J. Appl. Ceram. Technol. 14 (2) (2017) 117–127, https://doi.org/10.1111/ijac.12633.
[66] P. Miranda, A. Pajares, E. Saiz, A.P. Tomsia, F. Guiberteau, Mechanical properties of calcium phosphate scaffolds fabricated by robocasting, J. Biomed. Mater. Res. - Part A 85 (1) (2008) 218–227, https://doi.org/10.1002/jbm.a.31587.
[67] P. Miranda, A. Pajares, E. Saiz, A.P. Tomisa, F. Guiberteau, Fracture modes under uniaxial compression in hydroxyapatite scaffolds fabricated by robocasting, J. Biomed. Mater. Res. 83A (2007) 646–655, https://doi.org/10.1002/jbm.a.
[68] S. Ishack, A. Mediero, T. Wilder, J.L. Ricci, B.N. Cronstein, Bone regeneration in critical bone defects using three-dimensionally printed β-tricalcium phosphate/hydroxyapatite scaffolds is enhanced by coating scaffolds with either dipyridamole or BMP-2, J. Biomed. Mater. Res. - Part B Appl. Biomater. 105 (2) (2017) 366–375, https://doi.org/10.1002/jbm.b.33561.
[69] M. Mohammadi, et al., Robocasting of single and multi-functional calcium phosphate scaffolds and its hybridization with conventional techniques: design, fabrication and characterization, Appl. Sci. 10 (23) (2020) 1–22, https://doi.org/10.3390/app10238677.
[70] B. Nan, S. Olhero, R. Pinho, P.M. Vilarinho, T.W. Button, J.M.F. Ferreira, Direct ink writing of macroporous lead-free piezoelectric Ba 0.85 Ca 0.15 Zr 0.1 Ti 0.9 O 3, J. Am. Ceram. Soc. 102 (6) (2019) 3191–3203, https://doi.org/10.1111/jace.16220.
[71] J.E. Smay, S.S. Nadkarni, J. Xu, Direct writing of dielectric ceramics and base metal electrodes, Int. J. Appl. Ceram. Technol. 4 (1) (2007) 47–52, https://doi.org/10.1111/j.1744-7402.2007.02118.x.
[72] D. Brazete, A.S. Neto, J.M.F. Ferreira, Optimization of zirconia inks to fabricate 3D porous scaffolds by robocasting, Lek. a Tech. 49 (1) (2019) 5–10.
[73] T. Schlordt, F. Keppner, N. Travitzky, P. Greil, Robocasting of alumina lattice truss structures, J. Ceram. Sci. Technol. 3 (2) (2012) 81–88, https://doi.org/10.4416/JCST2012-00003.
[74] Z. Fu, M. Freihart, L. Wahl, T. Fey, P. Greil, N. Travitzky, Micro- and macroscopic design of alumina ceramics by robocasting, J. Eur. Ceram. Soc. 37 (9) (2017) 3115–3124, https://doi.org/10.1016/j.jeurceramsoc.2017.03.052.
[75] Y. Sun, C. Peng, X. Wang, R. Wang, Y. Chen, D. Zhang, Phase behavior of polyelectrolyte complexes and rheological behavior of alumina suspensions for direct ink writing, J. Am. Ceram. Soc. 99 (6) (2016) 1902–1910, https://doi.org/10.1111/jace.14155.
[76] Y. Sun, C. Peng, X. Wang, R. Wang, J. Yang, D. Zhang, Rheological behavior of Al2O3 suspensions containing polyelectrolyte complexes for direct ink writing, Powder Technol. 320 (2017) 223–229, https://doi.org/10.1016/j.powtec.2017.07.049.
[77] A. Goulas, et al., Additively manufactured ultra-low sintering temperature, low loss Ag2Mo2O7 ceramic substrates, J. Eur. Ceram. Soc. 41 (1) (2021) 394–401, https://doi.org/10.1016/j.jeurceramsoc.2020.08.031.
[78] I.H. Jo, Y.H. Koh, H.E. Kim, Coextrusion-based 3D plotting of ceramic pastes for porous calcium phosphate scaffolds comprised of hollow filaments, Materials (Basel) 11 (6) (2018), 911, https://doi.org/10.3390/ma11060911.
[79] S. Eqtesadi, A. Motealleh, P. Miranda, A. Lemos, A. Rebelo, J.M.F. Ferreira, A simple recipe for direct writing complex 45S5 Bioglass® 3D scaffolds, Mater. Lett. 93 (2013) 68–71, https://doi.org/10.1016/j.matlet.2012.11.043.
[80] J.E. Smay, G.M. Gratson, R.F. Shepherd, J. Cesarano, J.A. Lewis, Directed colloidal assembly of 3D periodic structures, Adv. Mater. 14 (18) (2002) 1279–1283, https://doi.org/10.1002/1521-4095(20020916)14:18<1279::AID-ADMA1279>3.0.CO;2-A.
[81] S.L. Morissette, J.A. Lewis, J. Cesarano, D.B. Dimos, T. Baer, Solid freeform fabrication of aqueous alumina-poly(vinyl alcohol) gelcasting suspensions, J. Am. Ceram. Soc. 83 (10) (2000) 2409–2416, https://doi.org/10.1111/j.1151-2916.2000.tb01569.x.
[82] H. Shao, J. He, T. Lin, Z. Zhang, Y. Zhang, S. Liu, 3D gel-printing of hydroxyapatite scaffold for bone tissue engineering, Ceram. Int. 45 (1) (2019) 1163–1170, https://doi.org/10.1016/j.ceramint.2018.09.300.
[83] D. Glymond, L.J. Vandeperre, Robocasting of MgO-doped alumina using alginic acid slurries, J. Am. Ceram. Soc. 101 (8) (2018) 3309–3316, https://doi.org/10.1111/jace.15509.
[84] Y. Chen, et al., A novel thixotropic magnesium phosphate-based bioink with excellent printability for application in 3D printing, J. Mater. Chem. B 6 (27) (2018) 4502–4513, https://doi.org/10.1039/c8tb01196f.
[85] Y. Luo, A. Lode, F. Sonntag, B. Nies, M. Gelinsky, Well-ordered biphasic calcium phosphate-alginate scaffolds fabricated by multi-channel 3D plotting under mild conditions, J. Mater. Chem. B 1 (33) (2013) 4088–4098, https://doi.org/10.1039/c3tb20511h.
[86] A. Lode, et al., Fabrication of porous scaffolds by three-dimensional plotting of a pasty calcium phosphate bone cement under mild conditions, J. Tissue Eng. Regen. Med. 8 (September (9)) (2014) 682–693, https://doi.org/10.1002/term.1563.
[87] T. Ahlfeld, et al., Design and fabrication of complex scaffolds for bone defect healing: combined 3D plotting of a calcium phosphate cement and a growth factor-loaded hydrogel, Ann. Biomed. Eng. 45 (1) (2017) 224–236, https://doi.org/10.1007/s10439-016-1685-4.
[88] S.L. Morissette, J.A. Lewis, P.G. Clem, J. Cesarano, D.B. Dimos, Direct-write fabrication of Pb(Nb,Zr,Ti)O3 devices: influence of paste rheology on print

morphology and component properties, J. Am. Ceram. Soc. 84 (11) (2001) 2462–2468, https://doi.org/10.1111/j.1151-2916.2001.tb01036.x.
[89] H. Elsayed, A. Chmielarz, M. Potoczek, T. Fey, P. Colombo, Direct ink writing of three dimensional Ti2AlC porous structures, Addit. Manuf. 28 (May) (2019) 365–372, https://doi.org/10.1016/j.addma.2019.05.018.
[90] H. Jin, D. Jia, Z. Yang, Y. Zhou, Direct ink writing of Si2N2O porous ceramic strengthened by directional β-Si3N4 grains, Ceram. Int. 46 (10) (2020) 15709–15713, https://doi.org/10.1016/j.ceramint.2020.03.077.
[91] H. Shao, et al., Bone regeneration in 3D printing bioactive ceramic scaffolds with improved tissue/material interface pore architecture in thin-wall bone defect, Biofabrication 9 (2) (2017), 025003, https://doi.org/10.1088/1758-5090/aa663c.
[92] X. Liu, M.N. Rahaman, G.E. Hilmas, B.S. Bal, Mechanical properties of bioactive glass (13-93) scaffolds fabricated by robotic deposition for structural bone repair, Acta Biomater. 9 (6) (2013) 7025–7034, https://doi.org/10.1016/j.actbio.2013.02.026.
[93] X. Shi, et al., Bioactive glass scaffold architectures regulate patterning of bone regeneration in vivo, Appl. Mater. Today 20 (2020) 100770, https://doi.org/10.1016/j.apmt.2020.100770.
[94] E. Feilden, et al., 3D printing bioinspired ceramic composites, Sci. Rep. 7 (2017), 13759, https://doi.org/10.1038/s41598-017-14236-9.
[95] A. Barba, et al., Osteoinduction by foamed and 3D-printed calcium phosphate scaffolds: effect of nanostructure and pore architecture, ACS Appl. Mater. Interfaces 9 (48) (2017) 41722–41736, https://doi.org/10.1021/acsami.7b14175.
[96] M. Houmard, Q. Fu, M. Genet, E. Saiz, A.P. Tomsia, On the structural, mechanical, and biodegradation properties of HA/β-TCP robocast scaffolds, J. Biomed. Mater. Res. - Part B Appl. Biomater. 101 (7) (2013) 1233–1242, https://doi.org/10.1002/jbm.b.32935.
[97] P. Diloksumpan, et al., Combining multi-scale 3D printing technologies to engineer reinforced hydrogel-ceramic interfaces, Biofabrication 12 (2) (2020), 025014, https://doi.org/10.1088/1758-5090/ab69d9.
[98] J. Lee, G. Kim, Calcium-deficient hydroxyapatite/collagen/platelet-rich plasma scaffold with controlled release function for hard tissue regeneration, ACS Biomater. Sci. Eng. 4 (1) (2018) 278–289, https://doi.org/10.1021/acsbiomaterials.7b00640.
[99] W.J. Kim, H.S. Yun, G.H. Kim, An innovative cell-laden α-TCP/collagen scaffold fabricated using a two-step printing process for potential application in regenerating hard tissues, Sci. Rep. 7 (2017), 3181, https://doi.org/10.1038/s41598-017-03455-9.
[100] N. Raja, A. Sung, H. Park, H. suk Yun, Low-temperature fabrication of calcium deficient hydroxyapatite bone scaffold by optimization of 3D printing conditions, Ceram. Int. 47 (5) (2020) 7005–7016, https://doi.org/10.1016/j.ceramint.2020.11.051.
[101] N. Raja, H.S. Yun, A simultaneous 3D printing process for the fabrication of bioceramic and cell-laden hydrogel core/shell scaffolds with potential application in bone tissue regeneration, J. Mater. Chem. B 4 (27) (2016) 4707–4716, https://doi.org/10.1039/c6tb00849f.
[102] M.M. Farag, H.S. Yun, Effect of gelatin addition on fabrication of magnesium phosphate-based scaffolds prepared by additive manufacturing system, Mater. Lett. 132 (2014) 111–115, https://doi.org/10.1016/j.matlet.2014.06.055.
[103] J.R.G.E. Hongyi Yang, Shoufeng Yang, Xiaopeng Chi, Fine Ceramic Lattices Prepared by Extrusion Freeforming, Wiley Intersci. 83 (2) (2005) 340–344, https://doi.org/10.1002/jbmb.
[104] A. Zocca, et al., Direct ink writing of a preceramic polymer and fillers to produce hardystonite (Ca2ZnSi2O7) bioceramic scaffolds, J. Am. Ceram. Soc. 99 (6) (2016) 1960–1967, https://doi.org/10.1111/jace.14213.
[105] H. Chen, X. Wang, F. Xue, Y. Huang, K. Zhou, D. Zhang, 3D printing of SiC ceramic: direct ink writing with a solution of preceramic polymers, J. Eur. Ceram. Soc. 38 (16) (2018) 5294–5300, https://doi.org/10.1016/j.jeurceramsoc.2018.08.009.
[106] T. An, K.T. Hwang, J.J.H. Kim, J.J.H. Kim, Extrusion-based 3D direct ink writing of NiZn-ferrite structures with viscoelastic ceramic suspension, Ceram. Int. 46 (5) (2020) 6469–6476, https://doi.org/10.1016/j.ceramint.2019.11.127.
[107] J. Maurath, N. Willenbacher, 3D printing of open-porous cellular ceramics with high specific strength, J. Eur. Ceram. Soc. 37 (15) (2017) 4833–4842, https://doi.org/10.1016/j.jeurceramsoc.2017.06.001.
[108] Y. Eom, F. Kim, S.E. Yang, J.S. Son, H.G. Chae, Rheological design of 3D printable all-inorganic inks using BiSbTe-based thermoelectric materials, J. Rheol. (N. Y. N. Y.) 63 (2) (2019) 291–304, https://doi.org/10.1122/1.5058078.
[109] A. Kumar, et al., Low temperature additive manufacturing of three dimensional scaffolds for bone-tissue engineering applications: processing related challenges and property assessment, Mater. Sci. Eng. R Rep. 103 (2016) 1–39, https://doi.org/10.1016/j.mser.2016.01.001.
[110] G.C. Papanicolaou, S.P. Zaoutsos, Viscoelastic Constitutive Modeling of Creep and Stress Relaxation in Polymers and Polymer Matrix Composites, Woodhead Publishing Limited, 2010.
[111] J. M. K, P. B. S. K, Abhijit P. Deshpande, Rheology of Complex Fluids, 2010.
[112] T. Chen, Rheological techniques for yield stress analysis. TA Instruments Tech. Notes - RH025, 2000, pp. 1–6.
[113] J. De Vicente, Rheology, 2012.
[114] J. Mewis, N.J. Wagner, Thixotropy, Adv. Colloid Interface Sci. 147–148 (2009) 214–227, https://doi.org/10.1111/j.1467-2494.1987.tb00472.x.
[115] F. Irgens, Rheology and non-Newtonian Fluids, vol. 9783319010, 2013.
[116] A. Schwab, R. Levato, M.D. Este, S. Piluso, D. Eglin, J. Malda, Printability and Shape Fidelity of Bioinks in 3D Bioprinting, Chem. Rev. 120 (19) (2020) 11028–11055, https://doi.org/10.1021/acs.chemrev.0c00084.
[117] J. Kutin, I. Bajsić, Fluid-dynamic loading of pipes conveying fluid with a laminar mean-flow velocity profile, J. Fluids Struct. 50 (2014) 171–183, https://doi.org/10.1016/j.jfluidstructs.2014.05.014.
[118] M. Jalaal, G. Cottrell, N. Balmforth, B. Stoeber, On the rheology of Pluronic F127 aqueous solutions, J. Rheol. (N. Y. N. Y.) 61 (1) (2017) 139–146, https://doi.org/10.1122/1.4971992.
[119] J. Graczyk, W.G. Gleißle, H. Buggisch, Rheological investigation of suspensions and ceramic pastes: characterization of extrusion properties, KONA Powder Part. J. 11 (ll) (1993) 125–137, https://doi.org/10.14356/kona.1993015.
[120] J. Bruneaux, D. Therriault, M.C. Heuzey, Micro-extrusion of organic inks for direct-write assembly, J. Micromech. Microeng. 18 (11) (2008), 115020, https://doi.org/10.1088/0960-1317/18/11/115020.
[121] Malvern Instruments, Understanding yield stress measurements, Annu. Trans. Nord. Rheol. Soc. 21 (2012) 6.
[122] Q. Sun, et al., Fabrication of 3D structures via direct ink writing of kaolin/graphene oxide composite suspensions at ambient temperature, Ceram. Int. 45 (15) (2019) 18972–18979, https://doi.org/10.1016/j.ceramint.2019.06.136.
[123] Y. Sun, C. Peng, X. Wang, R. Wang, J. Yang, D. Zhang, Rheological behavior of Al2O3 suspensions containing polyelectrolyte complexes for direct ink writing, Powder Technol. 320 (2017) 223–229, https://doi.org/10.1016/j.powtec.2017.07.049.
[124] N. Paxton, W. Smolan, T. Böck, F. Melchels, J. Groll, T. Jungst, Proposal to assess printability of bioinks for extrusion-based bioprinting and evaluation of rheological properties governing bioprintability, Biofabrication 9 (4) (2017), 044107, https://doi.org/10.1088/1758-5090/aa8dd8.
[125] Y. Eom, F. Kim, S.E. Yang, J.S. Son, H.G. Chae, Rheological design of 3D printable all-inorganic inks using BiSbTe-based thermoelectric materials, J. Rheol. (N. Y. N. Y.) 63 (2) (2019) 291–304, https://doi.org/10.1122/1.5058078.
[126] C.C. Hopkins, J.R. de Bruyn, Gelation and long-time relaxation of aqueous solutions of Pluronic F127, J. Rheol. (N. Y. N. Y.) 63 (1) (2019) 191–201, https://doi.org/10.1122/1.5054598.
[127] S. Salinas-Fernández, M. Santos, M. Alonso, L. Quintanilla, J.C. Rodríguez-Cabello, Genetically engineered elastin-like recombinamers with sequence-based molecular stabilization as advanced bioinks for 3D bioprinting, Appl. Mater. Today 18 (2020), 100500, https://doi.org/10.1016/j.apmt.2019.100500.
[128] G. Gillispie, et al., Assessment methodologies for extrusion-based bioink printability, Biofabrication 12 (2) (2020), 022003, https://doi.org/10.1088/1758-5090/ab6f0d.
[129] E. Feilden, Additive Manufacturing of Ceramics and Ceramic Composites Via Robocasting, 2017. https://spiral.imperial.ac.uk/handle/10044/1/55940.
[130] A. Ribeiro, et al., Assessing bioink shape fidelity to aid material development in 3D bioprinting, Biofabrication 10 (1) (2018), 014102, https://doi.org/10.1088/1758-5090/aa90e2.
[131] E.O. Osidak, et al., Viscoll collagen solution as a novel bioink for direct 3D bioprinting, J. Mater. Sci. Mater. Med. 30 (3) (2019), 31, https://doi.org/10.1007/s10856-019-6233-y.
[132] D. Petta, D.W. Grijpma, M. Alini, D. Eglin, M. D'Este, Three-dimensional printing of a tyramine hyaluronan derivative with double gelation mechanism for independent tuning of shear thinning and postprinting curing, ACS Biomater. Sci. Eng. 4 (8) (2018) 3088–3098, https://doi.org/10.1021/acsbiomaterials.8b00416.
[133] P.A. Comeau, T.L. Willett, Triethyleneglycol dimethacrylate addition improves the 3D-printability and construct properties of a GelMA-nHA composite system towards tissue engineering applications, Mater. Sci. Eng. C 112 (April) (2020), 110937, https://doi.org/10.1016/j.msec.2020.110937.
[134] N. Soltan, L. Ning, F. Mohabatpour, P. Papagerakis, X. Chen, Printability and cell viability in bioprinting alginate dialdehyde-gelatin scaffolds, ACS Biomater. Sci. Eng. 5 (6) (2019) 2976–2987, https://doi.org/10.1021/acsbiomaterials.9b00167.
[135] T. Gao, et al., Optimization of gelatin-alginate composite bioink printability using rheological parameters: a systematic approach, Biofabrication 10 (3) (2018), 034106, https://doi.org/10.1088/1758-5090/aacdc7.
[136] J. Malda, et al., 25th anniversary article: engineering hydrogels for biofabrication, Adv. Mater. 25 (36) (2013) 5011–5028, https://doi.org/10.1002/adma.201302042.
[137] A. Habib, V. Sathish, S. Mallik, B. Khoda, 3D printability of alginate-carboxymethyl cellulose hydrogel, Materials (Basel) 11 (3) (2018), 454, https://doi.org/10.3390/ma11030454.
[138] K.A. Deo, K.A. Singh, C.W. Peak, D.L. Alge, A.K. Gaharwar, Bioprinting 101: design, fabrication, and evaluation of cell-laden 3D bioprinted scaffolds, Tissue Eng. - Part A 26 (5–6) (2020) 318–338, https://doi.org/10.1089/ten.tea.2019.0298.
[139] H. Li, Y.J. Tan, S. Liu, L. Li, Three-dimensional bioprinting of oppositely charged hydrogels with super strong interface bonding, ACS Appl. Mater. Interfaces 10 (13) (2018) 11164–11174, https://doi.org/10.1021/acsami.7b19730.